
Article:
Finegan, T.M., Na, D., Cammarota, C. et al. (6 more authors) (2018) Tissue tension and not interphase cell shape determines cell division orientation in the Drosophila follicular epithelium. EMBO Journal, 37 (23). e100072. ISSN 0261-4189

10.15252/embj.2018100072

Tissue tension and not interphase cell shape determines cell division orientation in the Drosophila follicular epithelium

Tara M. Finegan[1], Daxiang Na[2], Christian Cammarota[3], Austin V. Skeeters[3], Tamás J. Nádasi[1], Nicole S. Dawney[1], Alexander G. Fletcher[4,5], Patrick W. Oakes[1,3], Dan T. Bergstralh[1,2,3,*]

[1]Department of Biology, University of Rochester, Rochester NY, 14627, [2]Department of Biomedical Genetics, University of Rochester Medical Center, Rochester, NY, 14627, USA, [3]Department of Physics & Astronomy, Rochester, NY, 14627, USA, and [4]School of Mathematics and Statistics, University of Sheffield, Sheffield, S3 7RH, UK, [5]Bateson Centre, University of Sheffield, Sheffield, S10 2TN, UK.

* Corresponding author
Correspondence: dan.bergstralh@rochester.edu

Running title: Shape-independent division orientation

Abstract

We investigated the cell behaviors that drive morphogenesis of the Drosophila follicular epithelium during expansion and elongation of early-stage egg chambers. We found that cell division is not required for elongation of the early follicular epithelium, but drives the tissue towards optimal geometric packing. We examined the orientation of cell divisions with respect to the planar tissue axis and found a bias towards the primary direction of tissue expansion. However, interphase cell shapes demonstrate the opposite bias. Hertwig's Rule, which holds that cell elongation determines division orientation, is therefore broken in this tissue. This observation cannot be explained by the anisotropic activity of the conserved Pins/Mud spindle-orienting machinery, which controls division orientation in the apical-basal axis, and planar division orientation in other epithelial tissues. Rather, cortical tension at the apical surface translates into planar division orientation in a manner dependent on Canoe/Afadin, which links actomyosin to adherens junctions. These findings demonstrate that division orientation in different axes - apical-basal and planar - is controlled by distinct, independent mechanisms in a proliferating epithelium.

Key words: Cell division / epithelia / morphogenesis / spindle orientation / tissue biology

Introduction

The remodeling of epithelial sheets is an essential process in animal embryonic development. Epithelial morphogenesis is a dynamic multiscale process that is the result of the coordination and integration of individual cell behaviors, including: shape change, rearrangement, division, extrusion and integration. Developing tissues utilize different combinations of these cell behaviors in distinct biological contexts to drive morphogenesis. The expansion and shaping of the Drosophila pupal notum and wing, and the mouse oral palate epithelium, are driven by the combined activity of cell division, rearrangement, shape changes and cell extrusion (Guirao et al, 2015). In contrast, salivary gland tube formation and germband extension in Drosophila embryos are driven by cell shape changes and cell rearrangements, with the latter process also including an additional small contribution from oriented cell divisions (reviewed in (Girdler & Röper, 2014; Kong et al, 2017)).

Morphogenetic cell behaviors are driven by the cell-intrinsic remodeling of the cytoskeleton, cell-cell adhesion factors and polarity domains. However, cell–extrinsic forces such as tissue-level tension also play a critical role in the induction of morphogenetic cell behaviors (Lye & Sanson, 2011). For example, the extrinsic force applied by the invagination of the posterior endoderm in the embryo induces shape changes and oriented junction growth needed for successful extension of the neighboring germband in the embryo (Lye et al, 2015; Collinet et al, 2015). We sought to explore the cell behaviors that drive morphogenesis of the follicular epithelium (FE), a simple, cuboidal monolayer. This tissue surrounds female germline cells in developing Drosophila egg chambers. Morphogenesis of the FE is characterized by gradual expansion with a directional bias. Therefore, the FE is a straightforward in vivo model to investigate the relationship between tissue elongation and morphogenetic cell behaviors.

As egg chambers mature during oogenesis, they increase in volume while simultaneously elongating (Fig 1A). Growth of the germline is independent of the FE, but polarized elongation of the egg chamber relies on the FE. There are two mechanisms whereby the FE promotes egg chamber elongation: firstly, it secretes a basement membrane extracellular matrix (ECM) which is stronger over the elongating bulk of the egg chamber than at the poles. This creates a gradient

of extracellular stiffness which biases expansion of the chamber in one direction (Crest et al, 2017). As the ECM is secreted, the FE collectively migrates along it, with individual follicle cells building and breaking ECM adhesions in a polarized manner, causing the egg chamber to rotate (Fig 1A') (Barlan et al, 2017; Cetera et al, 2014; Haigo & Bilder, 2011). Secondly, a morphogenetic gradient of JAK-STAT signaling across the FE, originating from polar cells, establishes a gradient of apical pulsatile contractions in the FE which contributes to elongation at early stages (Alégot et al, 2018).

The FE is proliferative as early changes in egg chamber shape and size take place. By convention, maturation of the egg chamber is divided into 14 stages. Between developmental stages 2 and 6/7, when mitoses cease, 4-5 rounds of division result in approximately 900 follicle cells (Horne-Badovinac & Bilder, 2005; Kolahi et al, 2009; Duhart et al, 2017; Klusza & Deng, 2011). These divisions are oriented with respect to the apical-basal axis, as they are in most epithelia, such that new cells are born within the tissue layer. Apical-basal division orientation is governed by a highly-conserved cortical machinery that includes Pins (Partner of Inscuteable) and Mud (Mushroom body defective). Mud uses dynein to exert a pulling force on astral microtubules, and thereby draws the mitotic spindle into alignment (reviewed in (di Pietro et al, 2016; Bergstralh et al, 2017)).

In this study, we addressed the question of how epithelial topology and shape develops in an elongating tissue. We determined that the tissue becomes increasingly regular as a consequence of proliferation, and that proliferation relieves stress exerted on the tissue by elongation. To achieve both of these goals, follicle cells in longer egg chambers must break Hertwig's Rule (translated as "the two poles of the division figure come to lie in the direction of the greatest protoplasmic mass", and also called the Long Axis Rule), orienting divisions contrary to the direction predicted by interphase cell shape cues (Hertwig, 1884). Instead, follicle cells achieve planar division orientation through a Mud-independent mechanism that relies on the mechanosensing of apical tension. This work demonstrates that tissues are not only distinct in the set of cell behaviors that drive epithelial morphogenesis, but that the mechanism which dictates the orientation of mitotic spindles, and therefore cell divisions, can vary between epithelial tissues within the same organism. We propose a biphasic model for spindle orientation in the FE by which apical-basal and planar orientation are uncoupled.

Results

The Follicle Epithelium Becomes Increasingly Regular Over Proliferative Stages of Egg Chamber Development

We examined the geometry of the FE in pre-vitellogenic egg chambers at proliferative stages, during which the aspect (long/short axis) ratios of egg chambers increases from approximately 1.0 to 1.6 (Cetera et al, 2014). We sought to identify how the FE develops to accommodate organ expansion and elongation. We took advantage of the fact that live egg chambers imaged in oil flatten perceptibly as they settle onto the coverslip (Fig 1B and B'), providing an area in which cells can be compared in two dimensions. This area is restricted to the central bulk of the egg chamber, over which elongation occurs, and excludes the terminal poles.

We used automated segmentation and image analysis to measure features of cell and tissue geometry using Basigin::YFP as a marker for cell membranes (Fig EV1A) and found that follicle cells decrease in cross-sectional area as egg chambers elongate (Fig 1C). Because the follicular epithelium is edgeless and expands as it develops, this result shows that the number of cells per unit tissue area is reduced, and therefore that cell proliferation outpaces organ elongation. The reduction in apical and basal cell surface area coincides with an increase in regularity (Fig 1D,E). We used cell circularity:

$$Circularity = 4\pi \times {Area}/{Perimeter^2}$$

as a measure of cell shape regularity because it depends on both cell perimeter and area and is therefore more sensitive to deviations in membrane shape than aspect ratio alone. We also frequently observed that cell height was uneven in these chambers (Fig EV1B). As these cells should not be different in terms of fate or polarity, this observation is indicative of inhomogeneous material properties or localized differences in tension, and indicate that cells can be deformed along the apical-basal axis by physiological-level forces.

As regularity increases, cells are more likely to be hexagonal (Fig 1D-E). We considered the possibility that cell geometry could change along the apical-basal (A-B) axis of the tissue, and therefore measured near to both the apical and basal tissue surfaces, but found that the

parameters we measured did not change significantly between them (Fig 1B-E). These measurements demonstrate that the FE transitions from a loosely organized state in very early egg chambers to a classic well-packed hexagonal 'honeycomb' by the time division stops at stage 6/7. This 'honeycomb' packing, identified by D'Arcy Thompson, is a common pattern in epithelia (Thompson, 1917).

Tissue Regularity, but not Elongation, Relies on Cell Division

These observations raise the question of how increased tissue regularity is coordinated with elongation. We addressed the importance of proliferation to elongation and topology by knocking down the cell cycle regulator String (Drosophila Cdc25) in the FE over 24 hours, and thereby decreasing follicle cell number (Fig 2A and EV1C) (Jimenez et al, 1990). Growth and elongation of the egg chamber were unaffected over the stages examined, although gross epithelial defects, including gaps, appear in later stage egg chambers (Figs 2A,B and EV1D-F). These results demonstrate that egg chamber elongation does not rely on increased follicle cell proliferation, and suggest that the increase in cell number is required to maintain an epithelial covering for the egg chamber as it matures. We also measured the effect of reduced proliferation on epithelial cell shape. Measurements of cell circularity and sidedness demonstrate that String-shRNA prevents the FE from increasing in regularity as the egg chamber elongates (Fig 2C,D). We conclude that tissue packing regularity in the FE, as in other systems, emerges as a consequence of proliferation (Gibson et al, 2006).

The Follicular Epithelium is Under Anisotropic Tension

Epithelial tissues exhibit active viscoelastic material properties and both generate and respond to mechanical stresses. Follicle cells at egg chamber poles exhibit different shapes and dynamic pulsatile behaviors at their apical surfaces than follicle cells at the equator (Alégot et al, 2018). This observation is consistent with the possibility of differences in the tension and/or material properties of the cortex between these locations. As the egg chamber is under internal pressure from the growth of nurse cells, follicle cells and the basal ECM exert forces to balance the expansionary pressure (Koride et al, 2014). Tissue-level tension is an important influencing factor in morphogenetic behaviors in other elongating tissues (Lecuit et al, 2011).

Consistent with the possibility that the egg chamber is under tension, we observed that follicle cell shape is changed in String-shRNA egg chambers. Firstly, cell areas increase in cross section (Fig 3A,B). Secondly, cell shapes change orientation, tending to align towards the long axis of the egg chamber (Fig 3C). Tissue "height" (length along the apical-basal axis) is a gradient in these egg chambers, with the shortest tissue over the equator and the tallest at the anterior and posterior poles (Fig 3D,E and EV2A). The extent of this gradient increases as the egg chamber elongates. These observations suggest that there is a gradient of tissue tension that is strongest at the middle of the egg chamber, and that the String-shRNA FE stretches to compensate for the decrease in cell number. We suggest two possibilities regarding the physical characteristics of the tissue: 1) tension is anisotropic across the egg chamber, with tension higher at the equator than the poles; 2) the mechanical properties of cells are different at the equator versus the poles (if the cells in the middle were less stiff, they would stretch first under uniform tension).

As in early stage egg chambers, we frequently observed that cell height is uneven in the stretched lateral cells, indicating that the cells are not under uniform tension (Fig 2A, box and Fig S2C,D). These observations suggest that follicle cells are capable of withstanding substantial mechanical deformation, consistent with observations made in older wt egg chambers. At stage 9, the post-mitotic epithelium at the anterior transitions from cuboidal to squamous, with a dramatic increase in individual follicle cell area. Our results agree with previous work suggesting that this change in morphology can be attributed to mechanical stress (Kolahi et al, 2009).

To test for a gradient of tension across the FE, we measured tissue recoil after severing the apical surface of the follicle cell epithelium (marked with Sqh-GFP) with a laser (Fig 3F). After 5 seconds the size of the wound at the apical cortex was consistently and significantly larger at cells located at the equator versus the poles (Fig 3G, EV2B). This result is consistent with the hypothesis that tension in the egg chamber is higher over the equator. However, we cannot rule out the possibility that the observed difference in cut size reflects differences in stiffness and viscosity of the cortex between these locations, since either of those properties will affect recoil dynamics.

To probe if there is anisotropy in the direction of apical tension, we performed a second laser ablation experiment where we made larger, circular cuts in the apical cortex of egg chambers at

stages 5 and 6 with aspect ratios greater than 1.35, taking advantage of a flattening-out of the tissue at the equator of the egg chamber when imaged live (Fig 1B', Fig 3H,I). Recoil was higher in the anterior-posterior (elongating / AP), compared to the up-down (rotating / UD) direction in 15 out of 20 cuts (Fig 3I and EV2C,D). There was large variability in the ratio of recoil in the AP and UD directions between cuts (Fig 3I and EV2D). This was not observed in ablations performed on egg chambers with aspect ratios of less 1.3. In these rounder egg chambers, recoil did not show a bias towards any axis and variability was lower (Fig EV2E). These results are consistent with an increase in global anisotropy in tension towards the AP/elongating axis of the egg chamber as the egg chamber elongates, but indicates that there are localized variances in tension across the tissue.

Together, our results show that there is an anisotropy in apical tension across the length of the egg chambers at elongated stages, with apical tension higher at the equator in comparison to the poles of the egg chamber and a global bias in tension towards the AP/elongating axis.

Planar Division Orientation in the FCE is Biased in the Direction of Tissue Expansion, not Interphase Cell Shape

Because the tissue is expanding directionally, packing in the FE must be under an additional level of control beyond the unbiased addition of cells. We considered four possible mechanisms: 1) cells are eliminated in overcrowded regions of the tissue; 2) the rate of proliferation varies across the tissue; 3) cells undergo rearrangements, 4) the orientation of cell divisions, and therefore the spatial addition of daughter cells into the tissue, is biased. We and others have failed to observe apoptosis in the FE, with the exception of several (<5) supernumerary polar cells lost by stage 5 (Besse & Pret, 2003; Bergstralh et al, 2015). We also failed to observe a substantial bias in division position, and we have never observed cell rearrangements prior to Stage 7 (Fig EV2F and EV Movie 1). Therefore, we discounted mechanisms 1, 2, and 3 in the early morphogenesis of the FE.

We next addressed the possibility that cell division orientations in the early FE are biased. We approximated the primary direction of tissue expansion through simple vector addition of the egg chamber long and short axes (Fig 4A). This results in an angle (relative to the long axis) that

decreases with developmental time, since the egg chamber becomes longer at a faster rate than it widens (Fig 4Bii). We found that the average division angle likewise decreases, becoming significantly different from random at Stage 6 (Fig 4Bi)**.** The distribution of these angles is wide, suggesting that the observed bias represents a granular property of the tissue rather than a planar polarized program for division orientation. While an earlier study failed to detect a bias in the orientation of planar cell divisions, developmental stage was not accounted for in that work (Alégot et al, 2018). However, planar division orientation analysis consistent with our data was reported in a preprinted article posted during the revision period of our manuscript (Chen et al, 2018).

We next considered whether the bias in division orientation is driven by egg chamber shape change. We tested this possibility by disrupting Fat2 (previously Kugelei), which is required for egg chamber rotation (Viktorinová et al, 2009; Cetera et al, 2014). We determined egg chamber stage by calculating volume, with adjustments based on nuclear staining pattern, and by defining the switch between 6 and 7 as the cessation of follicle cell mitoses (Klusza & Deng, 2011; Ng et al, 2016). Using this method, we found that Fat2-shRNA egg chambers are modestly, but significantly, less elongated than wild-type egg chambers at Stage 6 (Fig 4C, EV2G,H). This finding is consistent with earlier studies showing that disruption of Fat2, Abelson interacting protein, or SPARC (Secreted Protein Acidic and Rich in Cysteine), all of which regulate rotation or basement membrane deposition, inhibits elongation at Stage 6 (Cetera et al, 2014; Aurich & Dahmann, 2016). Unlike wild type egg chambers, cell division orientation is not significantly different from random in Fat2-shRNA egg chambers at Stage 6 (Fig 4C, EVB). We also failed to see a division orientation bias in Pak-shRNA egg chambers, which are significantly rounder at Stage 6 because of a defect in actomyosin contractility (Fig 4C, EV2H) (Vlachos & Harden, 2011). Together, these results are consistent with a model in which egg chamber shape and/or actomyosin contractility regulates division orientation.

In a tissue under tension, regularity can be achieved through a bias in the direction of cell division, such that new daughter cells are likely to appear along the stretch axis (Wyatt et al, 2015). Through this mechanism, local tension is relieved (Mao et al, 2013; Wyatt et al, 2015; Campinho et al, 2013). In the Drosophila wing disc and pupal notum, and during zebrafish epiboly, localized cortical tension is reflected in cell shape; tension causes interphase cells to

deform, giving them a long-cell axis at the apical tissue surface (Mao et al, 2013; Campinho et al, 2013; Bosveld et al, 2016). Interphase deformation has also been observed in a cultured cell system under stretch (Wyatt et al, 2015). We considered the possibility that interphase cell shape determines cell division orientation in egg chambers. We would expect apical shape to have a stronger impact on cell division for two reasons. First, mitotic cells in the FE frequently pull away from the basement membrane before dividing, and we show here that these detached cells can be physically excluded from the basal surface by neighboring follicle cells, which adjust to form attachments underneath them (Fig 4D) (Bergstralh et al, 2015). Second, planar orientation in the wing disc, pupal notum, and embryonic mesectoderm is determined by cortical tension at the apical tissue surface (Bosveld et al, 2016; Mao et al, 2013; Wang et al, 2017). In agreement with recent work, we found that follicle cell shapes are not oriented in the direction of tissue elongation but rather show a significant bias against it (Figs 4Biii,E) (Viktorinová et al, 2017). Furthermore, the extent of individual cell elongation correlates strongly with this directional bias (Fig EV2I). Cell shape is attributed to the collective cell migration that drives egg chamber rotation, which requires a traction force on basal cell surfaces (Cetera et al, 2014; Duhart et al, 2017; Haigo & Bilder, 2011; Viktorinová et al, 2017). The cell shape bias is the same at the apical and basal cell surfaces (Fig EV2J).

These findings suggest that cell division and cell shape are uncoupled in the follicular epithelium. To investigate this possibility, we imaged cell divisions live in the FE, and found that interphase cell shape elongation did not predict division angle (Fig 4F,G and EV Movie 2). Because our n is limited by slow growth of the tissue, we also examined the more rapidly dividing early embryonic neuroectoderm (stages 8-9) (henceforth ENE), and reached the same conclusion (Fig 4G).

Planar Spindle Orientation is Mud-Independent in the Follicular Epithelium

We next addressed the role of the canonical spindle-orienting machinery. We showed previously that Pins and Mud orient follicle cell spindles in the A-B axis, but did not address the possibility that they participate in planar division orientation (Bergstralh et al, 2013). In the imaginal wing disc and pupal notum, Mud localizes to vertices (junctions between three or more cells) throughout the cell cycle (Bergstralh et al, 2016; Bosveld et al, 2016). This pattern results in an

anisotropic distribution of the pulling force during mitosis, and translates the interphase long cell axis (at the apical surface) into planar division orientation (Bosveld et al, 2016). The position of cell vertices (Vertex Bipolarity) can therefore be used to predict division orientation in the wing disc/pupal notum (Bosveld et al, 2016). We did not find a relationship between Vertex Bipolarity and division orientation in either the FE or ENE (Fig 5A and EV3A). We also modified these calculations to take into account vertex distance from the cell center (Modified Vertex Bipolarity) but again found no relationship to division orientation (Fig 5A and EV3A). These observations may be explained by the composition of cell vertices. The wing disc and pupal notum are considered "mature," since they maintain specific protein complexes called tricellular junctions (TCJs) at the level of septate junctions at cell vertices. TCJs are necessary for Mud localization (Bosveld et al, 2016). Like the ENE at these stages, the FE is immature, since it does not demonstrate immunoreactivity to the TCJ marker Gliotactin (Fig EV3B,C) (Schulte et al, 2003). We examined Mud and Pins localization in the FE and ENE, and observed that both proteins localize around the entire mitotic cell cortex (Fig 5B,C and EV3D).

To test whether Mud plays a role in planar spindle orientation in the FE, we developed a suite of custom segmentation algorithms to distinguish egg chamber shapes, determine the egg chamber long axis, and calculate division angles relative to that axis based on manually-identified polar coordinates for the two spindle poles. We used this tool to analyze division orientation in Stage 5 and 6 egg chambers with an AR between 1.4 and 1.6 (Fig 5D) and found close agreement with our manual analysis (Fig 4B). A total of 52 control divisions were measured in this way. We found that the cell division angle mean is 31.6^{o}, with the division angle data significantly different from a hypothetical random data set with a median of 45^{o}. We also examined the distribution of a randomly generated set of numbers (0-90) of n = 50, and found that it is significantly different from wt division angles (Fig 5D). We disrupted Mud function using 1) the strong allele combination mud^{3}/mud^{4} and 2) Mud-shRNA (Bergstralh et al, 2015). We did not detect a defect in planar division orientation in either condition (Fig 5D and EV3E). As shown previously, Mud disruption caused misorientation of divisions with respect to the apical-basal axis (Fig EV5B); these out-of-plane division were excluded from our analysis, with a cutoff of >45° relative to the tissue surface. These results indicate that division orientation in the planar

axis is independent from the Pins/Mud machinery, which is consistent with the finding that Pins and Mud are evenly distributed around the mitotic cortex.

We used live imaging to determine the temporal dynamics of spindle orientation and observed that mitotic spindles can rotate in the plane after A-B orientation has been achieved (once both poles appear in the same tissue plane) (Fig 5E, EV3F-I and EV Movies 3,4). We quantified rotation in the rapidly developing ENE at stage 9, adapting the Spindlometer software to ensure that our quantifications were unbiased and consistent (Larson & Bement, 2017). Both the time over which spindles rotate in the plane of the tissue and the degree of spinning vary widely (Fig 5F, EV3F-I). However, as expected, spindles become closer to the division angle as they approach metaphase (Fig 5F). In some cases, the spindle exhibited oscillatory (rocking) behavior prior to metaphase (Fig EV3F-I). The finding that spindle orientation in the A-B and planar axes can be temporally separated suggests that they may have distinct mechanisms.

Apical Myosin Localization is Dynamic During Early Egg Chamber Development

Our results suggest a model in which division orientation is influenced by apicocortical tension. We therefore examined Myosin-II localization in the egg chamber, as marked by both Spaghetti Squash (Sqh; Drosophila Myosin Regulatory Light Chain II) and Zipper (Drosophila Myosin Heavy Chain II) (Fig 6A,B). Consistent with previous work, we observed that Myosin-II is enriched at the apical cortex (Fig EV4A). At Stages 3-5, Myosin-II exhibits a cellular-level organization, with clear junction and medial pools (Fig 6A,B, EV4B). By Stage 6 it exhibits a higher-order organization characterized by ‘nodes’ where fibers of Myosin coalesce and the inability to clearly distinguish the cortex of individual cells (Fig 6A,B, EV4B). This pattern is unlike that observed in the well-studied embryonic ectoderm, which maintains distinct junctional and medial pools of Myosin over the course of dramatic tissue-level morphogenetic movements (Fig EV4C). The change in apical Sqh localization found in the FE coincides with the increase in tissue regularity (Fig 1D,E). Contrastingly, the alignment of basal fibers of actomyosin occurs earlier in development, preceding egg chamber elongation (Fig EV4B) (Viktorinová et al, 2017). Contraction forces generated by the actomyosin cortex influence epithelial cell shape, but we cannot determine whether this change in the distribution of apical myosin is causative, or a consequence of increased regularity.

We noticed distinct spots of Zipper positioned along some follicle cell lateral membranes. These foci are reminiscent of somatic cell ring canals, which arise from incomplete cytokinesis and might therefore be expected to demonstrate enrichment of Myosin. Consistent with this possibility, we observed that Spaghetti Squash (Sqh; Drosophila Myosin Regulatory Light Chain II) colocalizes with the ring canal marker Pavarotti along lateral membranes (Fig EV4D) (Airoldi et al, 2011). We did not observe any pattern suggesting an active role for ring canals in epithelial topology.

We also characterized the localization of proteins implicated in junctional tension: Shotgun (Shg; Drosophila E-Cadherin), Canoe (Cno; Drosophila Afadin), Ajuba (Jub) and Armadillo (Arm; Drosophila β-catenin). Shg, Cno, Arm and Jub localize in belts at adherens junctions across stages 1-6 with no obvious planar polarity (Fig EV4E-H). These results suggest that there are not patterned differences in junctional tension across the egg chamber axes, as found in the embryonic ectoderm during germband extension.

Canoe Regulates Myosin Organization and Spindle Orientation

Adherens junctions are responsible for mechanotransduction and mechanosensing in epithelial cells (reviewed in (Lecuit et al, 2011)). We therefore tested whether these structures participate in planar spindle orientation in the FE. Although we did not detect a significant role for Shotgun (Drosophila E-Cadherin) in planar spindle orientation (Fig EV5A), this result is difficult to interpret because the functionally redundant protein DN-Cadherin is also expressed in the FE during division stages (Tanentzapf et al, 2000).

The adaptor protein Canoe (Afadin in vertebrates) is part of the machinery that links the actomyosin cytoskeleton to adherens junctions in epithelial cells (Sawyer et al, 2009; 2011). In other epithelial tissues, the loss of Canoe/Afadin causes mislocalization of actomyosin and the ability of cells to respond to tension (Sawyer et al, 2009; 2011; Choi et al, 2016). We found that Sqh-GFP appears detached from cell-cell contacts in Canoe-shRNA egg chambers, as previously observed in canoe mutant embryos (Sawyer et al, 2009; 2011) (Fig 7A). This finding is consistent with a model in which Canoe helps to transmit tissue-level tension to the cell.

Canoe is reported to directly regulate the Pins/Mud machinery in cultured cells and asymmetrically dividing Drosophila cells (Wee et al, 2011; Speicher et al, 2008; Carminati et al, 2016; Johnston et al, 2013). This does not appear to be true in the FE, since spindle orientation in the A-B axis is normal in mitotic clones mutant for the null allele cno^{R2} (Fig EV5B). Moreover, Canoe is not proximal to spindle poles (Fig EV5C). However, Canoe-shRNA follicle cells in Stage 6 exhibit planar division angles that are significantly different from wild type (Fig 7B). (Immunostaining was used to confirm that Canoe-shRNA depletes Canoe protein expression (Fig EV5D).) Although the orientation of cell divisions is abnormal, tissue elongation is normal in Canoe-shRNA treated egg chambers (Fig EV5E). Together, these results suggest that Canoe-shRNA decreases the bias in planar cell division by disrupting apical actomyosin-dependent tension.

We next examined the impact of planar division orientation on tissue topology. We first built a computational model for cell division in a stretched tissue. Because the bias in planar spindle orientation is not significant until Stage 6, which is also the stage at which follicle cell division ends, we simulated only one cell doubling. We modeled three conditions: division biased towards the stretch axis, 30° off the stretch axis (reflecting the difference between observed spindle angle and the interphase shape prediction), and random. Cell areas in our simulation decreased by roughly half, in agreement with a rate of proliferation that outpaces tissue expansion (Fig EV5F). We observed that division promoted optimal packing (hexagonality) in the stretch bias condition, and this effect was disrupted by division misorientation (Fig 7C). Consistent with the computational model, cell size was not appreciably different after Canoe disruption (Fig EV5G). However, follicle cells in egg chambers with aspect ratios 1.4-1.6 were less likely to be hexagonal than in wt (Fig 7D,E). Although we cannot rule out that disruption of Myo-II underlies the difference in tissue geometry we see when Canoe is disrupted, together with our results from String-shRNA egg chambers (Fig 2C,D), our data suggest that tension-driven division orientation contributes to regular tissue packing.

Discussion

Our results demonstrate that planar cell division orientation in the FE is independent of Pins/Mud. Instead, it relies on tissue tension and Canoe, which links actomyosin-based cortical tension to the cell. These findings show that division orientation occurs independently in the apical-basal and planar tissue axes (Fig 8). Although we have not investigated the effects of tension modulation or Canoe disruption in the embryonic ectoderm, our data suggest that bimodal spindle orientation is common to immature epithelia.

We propose that on the tissue scale, tension is oriented towards the elongation axis, but local anisotropies in the cortex, which could be stochastic or the consequence of cell behaviors, cause local differences in the tension exerted on individual cells. This is consistent with a model whereby division orientation is not dictated by an intrinsic genetic or developmental program, but is instead mediated by extrinsic physical factors. This bias in division orientation is a granular property of the epithelium; the division angle of any one cell cannot be predicted based on tissue-level tension, but a population bias exists such that cells will have bias towards the axis of tissue elongation.

Our study raises the question of whether biphasic spindle orientation is special to the FE, or a broad feature of immature epithelia. In other tissues, cell shape reflects tissue-level tension and cell shape cues direct the orientation of the spindle to establish the cell division angle (Fink et al, 2011; Bosveld et al, 2016). We have previously observed that dividing cells can move apically, detaching from the basement membrane. A potential explanation for this movement is that it allows dividing cells to escape the migration force that drives cell shape. This raises the question of how, if not through cell shape, apical tension is communicated to the spindle orienting machinery in the FE. This question will form the basis of future work.

Materials and Methods

Drosophila mutants and marker stocks: The following mutant alleles and transgenic constructs have been described previously: mud^{3} and mud^{4} (Yu et al, 2006), cno^{R2} (Sawyer et al, 2009), sqh^{AX3} (Jordan & Karess, 1997), $pins^{p62}$ (David et al, 2005), Ubi-α-Tub-RFP (Basto et al, 2008), Ubi-α-Tub84B-GFP (Rebollo et al, 2004), Ubi-Abnormal spindles-GFP (Rujano et al, 2013), Ubi-Centrosomin-RFP (Basto et al, 2008), Ubi-Centrosomin-GFP (Conduit et al, 2010), Ubi-Pins-YFP, Basigin::YFP (Lowe et al, 2014; Bergstralh et al, 2015), Mud-GFP (Bosveld et al, 2016), Pavarotti-KLP::GFP (Minestrini et al., 2003), Ajuba::GFP (BDSC_56806), Shotgun::GFP (Huang et al, 2009), Armadillo-GFP (McCartney et al, 2001), Spaghetti squash-mCherry (Martin et al, 2009), Zipper::YFP (Lowe et al, 2014). We thank the Transgenic RNAi Project at Harvard Medical School (NIH/NIGMS R01-GM084947) for UAS-Cno-shRNA (HMS00239), UAS-String-shRNA (HMS00146), UAS-Shg-shRNA (HMS00693), UAS-Mud-shRNA (HMS01458), UAS-Pak-shRNA (HMS02279) and UAS-Fat2-shRNA (HMS02136). The following background stocks were used to generate mitotic clones, which were induced by heat shock at 37° for multiple periods of two hours: RFP-nls, hsflp, FRT19A and hsflp; FRT40A RFP-nls, and hsflp;; FRT82B RFP-nls. Ectopic expression in follicle cells was driven by Traffic Jam-Gal4 (Olivieri et al, 2010), or actin5c-FLPout-Gal4, UAS-GFP (Fig. S4G only). For the String-shRNA experiments, flies developed to adulthood at 18°C, and were transferred to 29°C for 24 hours. For the Canoe-shRNA, Shg-shRNA, Pak-shRNA and Fat-shRNA experiments, flies were incubated at 29°C for 48 hours.

Reagents: The following antibodies were used in this study: rabbit anti-Canoe (gift from M. Peifer) (Sawyer et al, 2009), rabbit anti-Centrosomin (gift from J. Raff) (Lucas & Raff, 2007), rabbit anti-Mud (gift from R. Basto) (Rujano et al, 2013), rabbit anti-Pins (gift from F. Matsuzaki) (Izumi et al, 2006), rabbit anti-Gliotactin (gift from V. Auld), mouse anti-Armadillo (Developmental Studies Hybridoma Bank, N2 7A1 ARMADILLO, 12/10/15), and mouse FITC-conjugated anti-α-tubulin (Sigma, clone DM1A, Lot#114M4817V). Conjugated secondary antibodies were purchased from Thermo Fisher Scientific. Phalloidin was purchased from Invitrogen and Vectashield with DAPI was purchased from Vector Labs. Primary and secondary antibodies were used at a concentration of 1:150.

Imaging: Live cell imaging was performed in 10S halocarbon oil (egg chambers and embryos), or Schneider's medium (wing discs), as previously described (Bergstralh et al, 2015). Both live- and fixed-tissue imaging were undertaken on a Leica SP5 (63x/1.4 HCX PL Apo CS Oil). For live imaging in three dimensions, z-stacks of planes spaced 0.5μm apart were taken at one-minute intervals. Live imaging of Sqh-GFP was undertaken on a Nikon Ti-E inverted microscope coupled to an Andor Dragonfly 500 Confocal unit and Zyla 4.2 sCMOS camera using a 60x 1.49NA TIRF objective. Image collection and processing (Gaussian blur) were performed with Leica LAS AF and ImageJ.

Topology Measurements: The long and short axes of the egg chamber were determined using the EllipseFitter macro for ImageJ. Apical and basal surfaces of the follicle cells were manually identified from acquired z-stacks. Follicle cell membranes were segmented using a custom Java macro written for use in ImageJ which included use of features from the Biovoxxel Toolbox for ImageJ (Brocher, 2015). Cells at the edge of the field of view were excluded from analysis. The area, circularity, aspect ratio and the angle of the cell long axis were calculated using the Analyze Particles tool. The cell long axis is identified in this method by fitting an ellipse of best fit, with the angle result giving the angle between the primary axis and a line parallel to the x-axis of the image, which was manually set to correspond to the AP axis of the egg chamber. The angle was then corrected to be between 0-90^{o}. The number of cell sides (vertices) was identified using the 'Neighbor analysis' macro from the Biovoxxel Toolbox using watershedding and Voronoi analysis. All of these measurements are based on at least three egg chambers, from three flies, per aspect ratio. Centrosome angles with respect to the long axis were calculated using Image J. Statistical analyses were performed using Prism (GraphPad).

Circumferential Cell Number and Tissue Height Analysis: These measurements were performed manually using ImageJ. The analyst was blinded to tissue genotype. Lateral FC height is an average of measurements at two opposing positions midway through the egg chamber.

Division Angle Analysis (Live Tissue): The long axis of the egg chamber was determined using EllipseFitter for ImageJ. Division angles were measured by drawing a line between the two centrosomes and determining the angle between this line and the long axis.

Vertex Distribution Analysis (Live Tissue): Vertex Distribution and the major axis of cell elongation were identified through automated, unbiased analysis. Images were segmented and the positions of cell barycenters, vertices and the vectors from the barycenters to the vertices were identified using a custom MatLab script. The unit vectors from the barycenter to the vertices of the cells were used to calculate the expected division axis ('Vertex Bipolarity') by use of the TCJ bipolarity matrix as defined in Bosveld et al (2016):

$$B = \sum_{n=1}^{N_{TCJ}} (\hat{u}_n \otimes \hat{u}_n)$$

where B is the TCJ bipolarity Matrix, N_{TCJ} is the TCJs, and $\hat{u}_n$ refers to the unit vector to the n^{th} TCJ. The principal eigenvector of the TCJ bipolarity matrix defines the predicted axis along which the cell will divide, while the relative difference of the eigenvalues helps to determine how favored this axis is compared to the orthogonal direction (not included). We also considered the possibility that the distance of vertices from the barycenter could influence the magnitude of the pulling force ('Modified Vertex Bipolarity'). To do this, a similar calculation of the TCJ bipolarity matrix was employed, with the only caveat being that the full vector was used as opposed to the unit vectors.

Division Angle Analysis (Fixed Tissue): Division angles were determined using algorithms custom written in Python3. Qualitatively, the spindle was rotated about the long axis of the egg chamber to produce a top down view centered on the midpoint of the spindle. The angle of division was then measured as the deviation of the spindle orientation from the long axis. Mathematically, images were first thresholded and segmented in each plane of a z-stack based upon the tubulin staining to create binary image stacks of the egg chamber. The long axis of the egg chamber was calculated using a covariance matrix of the second central moments of the thresholded images to determine the unit eigenvectors, which represent the directions of the volume's principal axes. The axis corresponding to the largest eigenvalue was taken as the long-axis of the egg chamber. To determine spindle orientations, centrosome positions in x, y, and z were manually recorded. The midpoint between each centrosome pair was calculated, and a line was drawn from the midpoint to the point where the long axis intersected with the edge of the egg chamber. From this, a unit vector was calculated which pointed from the spindle midpoint to

one end of the chamber. A plane of projection was defined by the orthogonal directions of the cross-product of this unit vector with that of the long-axis, and the long-axis itself. Each centrosome pair was projected onto this plane using a dot product between the spindle unit vector and the unit vectors defining the plane of projection, yielding the desired top-down view. The angle of deflection between the projected centrosome unit vector and the long-axis was calculated by taking the inverse tangent of the two components of the projected spindle unit vector. These analyses were performed by researchers (PWO and AVS) blind to egg chamber genotype. For consistency with live imaging, divisions at the egg chamber termini were excluded.

Spindle rotation analysis: Movies were acquired of the embryonic ectoderm over approximately 8 μm every 20 seconds for 30-60 mins. The two-channel images were processed in ImageJ, with a max projection taken of the Tub::RFP, Cnn::RFP channel and an average projection of the Bas::YFP channel. Noise was removed and smoothened from the movies using a consistent set of image processing steps. Mitotic cells that could be followed from interphase to cytokinesis with consistently visible spindle poles and microtubules were selected and analyzed using the Spindlometer (Larson & Bement, 2017). Each orientation was tested against the previous measured orientation for angular differences of greater than 130 degrees. If there was a reported angle change of this magnitude, the point would be corrected by ±180 degrees. The angle at metaphase was set to 0 degrees at time 0 seconds, so that all cells could be compared using the same reference point.

Laser ablations: Ablations were performed on egg chambers from sqh^{AX3}, sqh::GFP flies. Cuts in the sagittal view were performed on a 2 photon system consisting of Olympus FV1000MPE and an Olympus Fluoview FVMPE-RS Twin Lasers Gantry System using an Olympus 25x 1.05NA objective lens with an Insight X3 laser tuned to 927 nm. The maximum laser power allowed to reach the sample was set to 220 mW. Images were collected every 0.5 s for 5 frames before the ablation and 20 frames after the ablation. Ablations were performed during image acquisition (with a dwell time of 10 μsec per pixel). Recoil was measured over a single pixel line ROI drawn over the curved apical surface. Recoil speed was calculated using the displacement of

the cut ends of the cortex between the first frame captured after ablation and a frame captured 5 seconds after the ablation.

Circular cuts in the apical surface of the tissue were performed using a Micropoint N2 laser (Andor) tuned to 435 nm. The laser delivers pulses of approximately 50 µJ, which are attenuated to reduce damage to minimize damage to surrounding tissue, at durations of 2–6 ns each. 1 laser pulse was applied to the tissue for cutting. Resulting tissue behavior was captured on a Nikon Ti-E inverted microscope coupled to an Andor Dragonfly 500 Confocal unit and Zyla 4.2 sCMOS camera using a 60x 1.49NA TIRF objective. Imaging was performed with a 50 mW 488nm laser. Recoil was measured across the circular cut by drawing 1-pixel wide lines parallel to the two chamber axes and using the displacement of the cut ends of the cortex between the first frame captured after ablation and a frame captured 5 seconds after the ablation.

Planar polarity measurements: Junctions from live confocal images of stage 6 egg chambers expressing junctional proteins tagged with fluorescent markers were traced by hand using FIJI. The line traces were expanded to 4 pixels wide and an average fluorescence intensity was taken across the length of the junction. Fluorescence intensity was normalized to the average cytoplasmic background pixel intensity. Intensity values were plotted against the orientation of junctions, corrected to fall between 0 and 90^{o} and normalized to the first group of angles.

Computational Model: We simulated a vertex model of the apical surface of the growing FE (Fletcher et al, 2014). Vertex models approximate cells in epithelial sheets as polygons representing the cells' apical surfaces, with vertices (points where three polygons meet) corresponding to adherens junctions. For simplicity, we neglected tissue curvature and instead simulated a two-dimensional planar tissue, imposing doubly periodic boundary conditions since the tissue is an edgeless epithelium. The model was non-dimensionalised such that all lengths and times were scaled with a typical cell diameter and by one hour, respectively. The position $\boldsymbol{r}_i(t)$ of each vertex i in the tissue was propagated over time according to the equation of motion

$$\eta \frac{d\boldsymbol{r}_i(t)}{dt} = \frac{\partial U}{\partial \boldsymbol{r}_i}(t). \qquad (1)$$

This equation was derived by balancing the force acting on each vertex due to surface tension, cortical contractility, and the combined effect of cell-cell adhesion and junctional contractility, with an effective viscous drag with associated coefficient $\eta = 0.04$. In equation (1), for the effective energy function U we employed the widely-used expression

$$U = \sum_{\alpha} \frac{K}{2}(A_\alpha - A_0)^2 + \sum_{\alpha} \frac{\Gamma}{2} {P_\alpha}^2 + \sum_{(i,j)} \Lambda l_{ij}. \qquad (2)$$

Vertex models using this description of cell mechanics have previously been shown to match observed junctional movements and cell shapes in epithelial sheets through validation against experimental measurements (Farhadifar et al, 2007). Here, A_α and P_α denote the apical surface area and perimeter of cell α, $A_0 = 1$ is a common 'target' area, l_{ij} is the length of the edge shared by vertices i and j, and the coefficients $K = 1$, $\Gamma = 0.04$, and $\Lambda = 0.12$ together govern the strength of the individual energy contributions. For this choice of parameters, regular hexagonal packing represents the unique ground state configuration, and work is required to compress, expand or shear the tissue (Farhadifar et al, 2007)**.**

As vertex positions were propagated according to (1), some cell-cell interfaces shrank to zero length. If this occurred, we implemented a cell neighbor exchange ('T1 transition'), replacing the old edge with a new perpendicular edge connecting those cells that were previously separated by the old edge.

We simulated the growth of the egg chamber by imposing a slow increase in the width and length of the doubly periodic domain, with speeds $s_x = 0.001$ and $s_y = 0.001/\sqrt{3}$ respectively. These values were chosen to approximately match the observed change in aspect ratio during the relevant stage of development.

The total number of vertices in each simulation changed over time, due to cell division. For simplicity, we assumed that cell cycle times were independent and randomly drawn from the uniform distribution with minimum $\tau_{min} = 3$ and maximum $\tau_{max} = 5$. These values were chosen to approximately match the observed increase in cell number in the FE during the relevant stage of development. When a cell was ready to divide, we created a new cell-cell interface at a specified angle θ to the x-axis through the centroid of the parent cell.

To explore the effect of division orientation in this model, we considered three alternative choices for the angle of division: (1) biased towards the stretch axis of the tissue, such that θ was independently drawn from the wrapped normal distribution with mean 30 degrees and variance 10 degrees; (2) randomised division, such that θ was independently drawn from the uniform distribution with minimum 0 degrees and maximum 180 degrees; (3) orientation perpendicular to the long axis of the parent cell (stretch axis bias). Here, we defined the long axis as passing through the centroid of the parent cell in the direction of the eigenvector corresponding to the larger eigenvalue of the inertial tensor (Fletcher et al, 2013).

Each model simulation started from an initial cell packing generated by computing the Voronoi tessellation of 36 seed points distributed uniformly at random in a square of width $L_0 = 6$, and relaxing this configuration to mechanical equilibrium. The tissue was then evolved over discrete time steps of length $\Delta t = 0.0001$ using an explicit Euler method. This size of time step was chosen to ensure numerical stability (Kursawe et al, 2017)**.** At each time step we: updated the age of each cell and implemented any divisions; performed a neighbor exchange for any cell-cell interface whose length dropped below $d_{min} = 0.01$, replacing it with a new orthogonal interface of length $1.5d_{min}$; removed any cell (T2 transition) whose area dropped below $A_{min} = 0.001$; used an explicit Euler method to integrate equation (1) and updated the positions of all vertices simultaneously; and increased the width and length of the periodic domain by $s_x\Delta t$ and $s_x\Delta t$ respectively, imposing a uniform strain across the tissue. Each simulation was halted as soon as each initial cell had divided once, at which time we recorded the area, circularity, and number of sides of each cell in the tissue. These data were used to calculate the summary statistics shown in Figs 7 and EV5. Simulations were implemented in the software Chaste (Fletcher et al, 2013; Mirams et al, 2013).

Acknowledgements: We are grateful to Holly Lovegrove and David Bilder for their useful comments during our study. We are also grateful to Tyler Wilson, Yurong Gao, Nick Reilly, Nick Weeks, and Allison Bhattacharya for technical assistance. We thank the Developmental Studies Hybridoma Bank at the University of Iowa and Transgenic RNAi Project (TRiP) at Harvard for antibodies and stocks.

Conflict of Interest: The authors declare no conflicts of interest.

Author Contributions: DTB conceived the project and designed the experiments. AGF designed the computational model and performed and analyzed the simulations. AVS and PWO designed the algorithms for fixed-tissue division analyses. DN, NSD, and DTB performed the imaging. TMF and DTB designed the analysis with help from CC and together with AVS, TN, CC and PWO analyzed the images. TMF and DTB wrote the manuscript.

Funding: This work was supported by internal funding from the University of Rochester including internal funding (SAC) to DTB, PWO, and B. Biteau. AGF is supported by a Vice-Chancellor's Fellowship from the University of Sheffield.

References

Airoldi SJ, McLean PF, Shimada Y & Cooley L (2011) Intercellular protein movement in syncytial Drosophila follicle cells. J Cell Sci **124:** 4077–4086

Aurich F & Dahmann C (2016) A Mutation in fat2 Uncouples Tissue Elongation from Global Tissue Rotation. Cell Reports **14:** 2503–2510

Barlan K, Cetera M & Horne-Badovinac S (2017) Fat2 and Lar Define a Basally Localized Planar Signaling System Controlling Collective Cell Migration. Dev Cell **40:** 467–477.e5

Basto R, Brunk K, Vinadogrova T, Peel N, Franz A, Khodjakov A & Raff JW (2008) Centrosome amplification can initiate tumorigenesis in flies. Cell **133:** 1032–1042

Bergstralh DT, Dawney NS & St Johnston D (2017) Spindle orientation: a question of complex positioning. Development **144:** 1137–1145

Bergstralh DT, Lovegrove HE & St Johnston D (2013) Discs large links spindle orientation to apical-Basal polarity in Drosophila epithelia. Curr Biol **23:** 1707–1712

Bergstralh DT, Lovegrove HE & St Johnston D (2015) Lateral adhesion drives reintegration of misplaced cells into epithelial monolayers. Nat Cell Biol

Bergstralh DT, Lovegrove HE, Kujawiak I, Dawney NS, Zhu J, Cooper S, Zhang R & St Johnston D (2016) Pins is not required for spindle orientation in the Drosophila wing disc. Development **143:** 2573–2581

Besse F & Pret A-M (2003) Apoptosis-mediated cell death within the ovarian polar cell lineage of Drosophila melanogaster. Development **130:** 1017–1027

Bosveld F, Markova O, Guirao B, Martin C, Wang Z, Pierre A, Balakireva M, Gaugue I, Ainslie A, Christophorou N, Lubensky DK, Minc N & Bellaïche Y (2016) Epithelial tricellular junctions act as interphase cell shape sensors to orient mitosis. Nature **530:** 495–498

Campinho P, Behrndt M, Ranft J, Risler T, Minc N & Heisenberg C-P (2013) Tension-oriented cell divisions limit anisotropic tissue tension in epithelial spreading during zebrafish epiboly. Nat Cell Biol **15:** 1405–1414

Carminati M, Gallini S, Pirovano L, Alfieri A, Bisi S & Mapelli M (2016) Concomitant binding of Afadin to LGN and F-actin directs planar spindle orientation. Nat Struct Mol Biol **23:** 155–163

Cetera M, Juan GRR-S, Oakes PW, Lewellyn L, Fairchild MJ, Tanentzapf G, Gardel ML & Horne-Badovinac S (2014) Epithelial rotation promotes the global alignment of contractile actin bundles during Drosophila egg chamber elongation. Nature Communications **5:** 5511

Chen D-Y, Crest J, Streichan SJ & Bilder D (2018) 3D Tissue elongation via ECM stiffness-

cued junctional remodeling. bioRxiv**:** 384958

Choi W, Acharya BR, Peyret G, Fardin M-A, Mège R-M, Ladoux B, Yap AS, Fanning AS & Peifer M (2016) Remodeling the zonula adherens in response to tension and the role of afadin in this response. J Cell Biol **213:** 243–260

Collinet C, Rauzi M, Lenne P-F & Lecuit T (2015) Local and tissue-scale forces drive oriented junction growth during tissue extension. Nat Cell Biol **17:** 1247–1258

Conduit PT, Brunk K, Dobbelaere J, Dix CI, Lucas EP & Raff JW (2010) Centrioles regulate centrosome size by controlling the rate of Cnn incorporation into the PCM. Curr Biol **20:** 2178–2186

Crest J, Diz-Muñoz A, Chen D-Y, Fletcher DA & Bilder D (2017) Organ sculpting by patterned extracellular matrix stiffness. Elife **6:** e24958

David NB, Martin CA, Segalen M, Rosenfeld F, Schweisguth F & Bellaïche Y (2005) Drosophila Ric-8 regulates Galphai cortical localization to promote Galphai-dependent planar orientation of the mitotic spindle during asymmetric cell division. Nat Cell Biol **7:** 1083–1090

di Pietro F, Echard A & Morin X (2016) Regulation of mitotic spindle orientation: an integrated view. EMBO Rep.**:** e201642292

Duhart JC, Parsons TT & Raftery LA (2017) The repertoire of epithelial morphogenesis on display: Progressive elaboration of Drosophila egg structure. Mech. Dev.

Farhadifar R, Röper J-C, Aigouy B, Eaton S & Jülicher F (2007) The Influence of Cell Mechanics, Cell-Cell Interactions, and Proliferation on Epithelial Packing. Current Biology **17:** 2095–2104

Fink J, Carpi N, Betz T, Bétard A, Chebah M, Azioune A, Bornens M, Sykes C, Fetler L, Cuvelier D & Piel M (2011) External forces control mitotic spindle positioning. Nat Cell Biol **13:** 771–778

Fletcher AG, Osborne JM, Maini PK & Gavaghan DJ (2013) Implementing vertex dynamics models of cell populations in biology within a consistent computational framework. Progress in Biophysics and Molecular Biology **113:** 299–326

Fletcher AG, Osterfield M, Baker RE & Shvartsman SY (2014) Vertex Models of Epithelial Morphogenesis. Biophysical Journal **106:** 2291–2304

Gibson MC, Patel AB, Nagpal R & Perrimon N (2006) The emergence of geometric order in proliferating metazoan epithelia. Nature **442:** 1038–1041

Guirao B, Rigaud SU, Bosveld F, Bailles A, López-Gay J, Ishihara S, Sugimura K, Graner F & Bellaïche Y (2015) Unified quantitative characterization of epithelial tissue development. Elife **4:** 773

Haigo SL & Bilder D (2011) Global tissue revolutions in a morphogenetic movement controlling elongation. Science **331:** 1071–1074

Hertwig O (1884) Untersuchungen zur Morphologie und Physiologie der Zelle: Das Problem der Befruchtung und der Isotropie des Eies, eine Theorie der Vererbung

Horne-Badovinac S & Bilder D (2005) Mass transit: epithelial morphogenesis in the Drosophila egg chamber. Dev. Dyn. **232:** 559–574

Huang J, Zhou W, Dong W, Watson AM & Hong Y (2009) From the Cover: Directed, efficient, and versatile modifications of the Drosophila genome by genomic engineering. **106:** 8284–8289

Izumi Y, Ohta N, Hisata K, Raabe T & Matsuzaki F (2006) Drosophila Pins-binding protein Mud regulates spindle-polarity coupling and centrosome organization. Nat Cell Biol **8:** 586–593

Jimenez J, Alphey L, Nurse P & Glover DM (1990) Complementation of fission yeast cdc2ts and cdc25ts mutants identifies two cell cycle genes from Drosophila: a cdc2 homologue and string. EMBO J **9:** 3565–3571

Johnston CA, Manning L, Lu MS, Golub O, Doe CQ & Prehoda KE (2013) Formin-mediated actin polymerization cooperates with Mushroom body defect (Mud)-Dynein during Frizzled-Dishevelled spindle orientation. J Cell Sci **126:** 4436–4444

Klusza S & Deng W-M (2011) At the crossroads of differentiation and proliferation: Precise control of cell-cycle changes by multiple signaling pathways in Drosophila follicle cells. Bioessays **33:** 124–134

Kolahi KS, White PF, Shreter DM, Classen AK, Bilder D & Mofrad MRK (2009) Quantitative analysis of epithelial morphogenesis in Drosophila oogenesis: New insights based on morphometric analysis and mechanical modeling. Developmental Biology **331:** 129–139

Kursawe J, Baker RE & Fletcher AG (2017) Impact of implementation choices on quantitative predictions of cell-based computational models. Journal of Computational Physics **345:** 752–767

Larson ME & Bement WM (2017) Automated mitotic spindle tracking suggests a link between spindle dynamics, spindle orientation, and anaphase onset in epithelial cells. Mol Biol Cell **28:** 746–759

Lecuit T, Lenne P-F & Munro E (2011) Force generation, transmission, and integration during cell and tissue morphogenesis. Annu. Rev. Cell Dev. Biol. **27:** 157–184

Lowe N, Rees JS, Roote J, Ryder E, Armean IM, Johnson G, Drummond E, Spriggs H, Drummond J, Magbanua JP, Naylor H, Sanson B, Bastock R, Huelsmann S, Trovisco V, Landgraf M, Knowles-Barley S, Armstrong JD, White-Cooper H, Hansen C, et al (2014) Analysis of the expression patterns, subcellular localisations and interaction partners of

Drosophila proteins using a pigP protein trap library. Development **141:** 3994–4005

Lucas EP & Raff JW (2007) Maintaining the proper connection between the centrioles and the pericentriolar matrix requires Drosophila centrosomin. Journal of Cell Biology **178:** 725–732

Lye CM & Sanson B (2011) Tension and epithelial morphogenesis in Drosophila early embryos. Curr. Top. Dev. Biol. **95:** 145–187

Lye CM, Blanchard GB, Naylor HW, Muresan L, Huisken J, Adams RJ & Sanson B (2015) Mechanical Coupling between Endoderm Invagination and Axis Extension in Drosophila. PLoS Biol. **13:** e1002292

Mao Y, Tournier AL, Hoppe A, Kester L, Thompson BJ & Tapon N (2013) Differential proliferation rates generate patterns of mechanical tension that orient tissue growth. EMBO J **32:** 2790–2803

Martin AC, Kaschube M & Wieschaus EF (2009) Pulsed contractions of an actin-myosin network drive apical constriction. Nature **457:** 495–499

McCartney BM, McEwen DG, Grevengoed E, Maddox P, Bejsovec A & Peifer M (2001) Drosophila APC2 and Armadillo participate in tethering mitotic spindles to cortical actin. Nat Cell Biol **3:** 933–938

Mirams GR, Arthurs CJ, Bernabeu MO, Bordas R, Cooper J, Corrias A, Davit Y, Dunn S-J, Fletcher AG, Harvey DG, Marsh ME, Osborne JM, Pathmanathan P, Pitt-Francis J, Southern J, Zemzemi N & Gavaghan DJ (2013) Chaste: An Open Source C++ Library for Computational Physiology and Biology. PLoS Comput. Biol. **9:** e1002970

Ng BF, Selvaraj GK, Santa-Cruz Mateos C, Grosheva I, Alvarez-Garcia I, Martín-Bermudo MD & Palacios IM (2016) α-Spectrin and integrins act together to regulate actomyosin and columnarization, and to maintain a monolayered follicular epithelium. Development **143:** 1388–1399

Olivieri D, Sykora MM, Sachidanandam R, Mechtler K & Brennecke J (2010) An in vivo RNAi assay identifies major genetic and cellular requirements for primary piRNA biogenesis in Drosophila. EMBO J **29:** 3301–3317

Rebollo E, Llamazares S, Reina J & Gonzalez C (2004) Contribution of noncentrosomal microtubules to spindle assembly in Drosophila spermatocytes. **2:** E8

Rujano MA, Sanchez-Pulido L, Pennetier C, le Dez G & Basto R (2013) The microcephaly protein Asp regulates neuroepithelium morphogenesis by controlling the spatial distribution of myosin II. Nat Cell Biol **15:** 1294–1306

Sawyer JK, Choi W, Jung K-C, He L, Harris NJ & Peifer M (2011) A contractile actomyosin network linked to adherens junctions by Canoe/afadin helps drive convergent extension. Mol Biol Cell **22:** 2491–2508

Sawyer JK, Harris NJ, Slep KC, Gaul U & Peifer M (2009) The Drosophila afadin homologue Canoe regulates linkage of the actin cytoskeleton to adherens junctions during apical constriction. J Cell Biol **186:** 57–73

Schulte J, Tepass U & Auld VJ (2003) Gliotactin, a novel marker of tricellular junctions, is necessary for septate junction development in Drosophila. Journal of Cell Biology **161:** 991–1000

Speicher S, Fischer A, Knoblich J & Carmena A (2008) The PDZ protein Canoe regulates the asymmetric division of Drosophila neuroblasts and muscle progenitors. Curr Biol **18:** 831–837

Tanentzapf G, Smith C, McGlade J & Tepass U (2000) Apical, lateral, and basal polarization cues contribute to the development of the follicular epithelium during Drosophila oogenesis. Journal of Cell Biology **151:** 891–904

Viktorinová I, Henry I & Tomancak P (2017) Epithelial rotation is preceded by planar symmetry breaking of actomyosin and protects epithelial tissue from cell deformations. PLoS Genet. **13:** e1007107

Viktorinová I, König T, Schlichting K & Dahmann C (2009) The cadherin Fat2 is required for planar cell polarity in the Drosophila ovary. Development **136:** 4123–4132

Vlachos S & Harden N (2011) Genetic Evidence for Antagonism Between Pak Protein Kinase and Rho1 Small GTPase Signaling in Regulation of the Actin Cytoskeleton During Drosophila Oogenesis. Genetics **187:** 501–512

Wang MFZ, Hunter MV, Wang G, McFaul C, Yip CM & Fernandez-Gonzalez R (2017) Automated cell tracking identifies mechanically oriented cell divisions during Drosophila axis elongation. Development **144:** 1350–1361

Wee B, Johnston CA, Prehoda KE & Doe CQ (2011) Canoe binds RanGTP to promote Pins(TPR)/Mud-mediated spindle orientation. J Cell Biol **195:** 369–376

Wyatt TPJ, Harris AR, Lam M, Cheng Q, Bellis J, Dimitracopoulos A, Kabla AJ, Charras GT & Baum B (2015) Emergence of homeostatic epithelial packing and stress dissipation through divisions oriented along the long cell axis. **112:** 5726–5731

Yu JX, Guan Z & Nash HA (2006) The mushroom body defect gene product is an essential component of the meiosis II spindle apparatus in Drosophila oocytes. Genetics **173:** 243–253

Figure Legends

Fig 1: Epithelial topology becomes increasingly regular as the early egg chamber matures.

A) Egg chambers expand and elongate through development. This is acheieved through collective migration (A') of the FE.

B) Egg chambers flatten along the coverslip, allowing for follicle cell morphologies to be compared in two dimensions. In (B), three live w^{1118} (control) egg chambers expressing the membrane marker Basigin::YFP are shown in multiple planes of focus, with a z-reconstruction at the bottom. Because the egg chambers flatten at the coverslip, the basal follicle cell morphologies can be revealed in a single focal plane. To account for differences in follicle cell height between the three egg chambers, which increase in maturity from left to right, separate focal planes are shown for the apical morphologies. A diagram illustrating the position of the three focal planes with respect to the flattened egg chamber is shown in (B'). Scale bars = 20 μm.

C–E) Follicle cell cross-sectional area decreases (C) and cell shape becomes more regular (D) and hexagonal (E) as early-stage egg chambers mature. These measurements were derived from at least three egg chambers from at least three flies per AR range. Bars in (C) and (D) represent mean and standard deviation. Statistical significance for cell side distributions was calculated using a chi-squared test. Number of cells used for morphological analysis: 1.0-1.2 apical n=23, basal n=27; 1.2-1.4 apical n=114, basal n=61; 1.4-1.6, apical n=160, basal n=149. Vertex counts: 1.0-1.2 apical n =38, basal n=33; 1.2-1.4 apical n=73, basal n=70; 1.4-1.6, apical n=284, basal n=259.

Fig 2: Tissue regularity is a function of cell proliferation.

A, B) Egg chamber elongation is unaffected by reduced cell proliferation. String-shRNA expressed for 24 hours alters epithelial shape and cell number (A), but not the relationship between egg chamber aspect ratio and cross-sectional area, which is quantified in (B). Chambers shown in (A) have approximately equal widths, with the cross-sectional area corresponding to developmental stage 6. Scale bars = 20 μm. Number of chambers analyzed: w^{1118} 1.0-1.2

n=24,1.2-1.4 n=14,1.4-1.6 n=18 String-shRNA 1.0-1.2 n= 11 ,1.2-1.4 n=10,1.4-1.6 n=15. Bars represent mean and standard deviation.

C, D) Cell proliferation is necessary for normal tissue morphology. Follicle cell shape regularity (C) and polygonality (D) measurements in control and String-shRNA egg chambers of different aspect ratios. These measurements were derived from at least three egg chambers from at least three flies per AR range. Bars represent mean and standard deviation. Statistical significance for cell side distributions was calculated using a chi-squared test. Number of cells used for analysis: w^{1118} 1.0-1.2 n= 23, 1.2-1.4 n=114, 1.4-1.6 n=160; String-shRNA 1.0-1.2, n=6, 1.2-1.4 n=19, 1.4-1.6 n=17.

Fig 3: The follicular epithelium is under anisotropic apical tension.

A-C) Epithelial cell size and shape is affected by decreased proliferation. Representative images of epithelial cells taken from egg chambers with aspect ratios of approximately 1.4 (A). Cell outlines are marked with Basigin::YFP. Scale bars = 5 μm. Cells become significantly larger (B) and more aligned with the tissue elongation axis when proliferation is stopped using String-shRNA (C). Cell area shown on a $\log_4$ scale in (B). Number of cells analyzed: w^{1118} 1.0-1.2 n= 14, 1.2-1.4 n=114, 1.4-1.6 n=160; String-shRNA 1.0-1.2, n=10, 1.2-1.4 n=19, 1.4-1.6 n=17. Statistical significance calculated using a Mann-Whitney test.

D, E) The follicular epithelium 'thins out' over the egg chamber equator when proliferation is blocked. Cartoon demonstrates the tissue cell shape observed in the follicular epithelium in control (w^{1118}) and String-shRNA treated egg chambers. Quantification of the phenomenon shown in (D) reveals that cells are shorter over the equator than at the anterior pole in elongated egg chambers when proliferation is blocked. Statistical significance calculated using unpaired t-test with Welch's correction. Number of cells analyzed: w^{1118} 1.0-1.2 n= 21, 1.2-1.4 n=11, 1.4-1.6 n=10; String-shRNA 1.0-1.2, n=9, 1.2-1.4 n=11, 1.4-1.6 n=13.

F) Recoil is observed when cuts are made in apical cortex with a 2-photon laser with egg chambers in saggital view. Images show cortex before and after cutting. Scale bars = 10 μm. Yellow arrows indicate edges of ablated region.

G) Recoil is higher when cuts are made at the apical cortex at the equator of egg chambers, rather than at the poles. Quantification of experiment shown in (F). Statistical significance tested by Mann-Whitney test. Number of laser cuts: equator n=30, pole n=20.

H) Recoil is observed when larger cuts are made in apical cortex with a UV laser. Images show cortex before and after cutting. Red lines indicate the lines over which recoil was calculated, parallel to the axes of the egg chamber. Scale bars = 5 μm. Yellow arrows indicate edges of ablated region.

I) Recoil tends to be higher towards the AP (elongation) axis compared to the the UD (rotation) axis. Graph shows the ratio of recoil speed plotted on a $\log_2$ scale in the AP versus the UD axis. Red line at x=1 indicates equal recoil in both axes. Values above 1 indicate higher recoil speeds in the AP axis lower than 1 indicate higher recoil in the UD axis. AP/UD Ratio Median = 1.242 ; Mean = 2.1. Wilcoxon Signed Rank Test to test for significance of the recoil ratio AP/UD shows that the median is significantly different from 1 to p = 0.0172. Number of cuts = 20. Bar represents median.

Data information: Bars in (B, C, E) represent mean and standard deviation. Laser ablation experiments in (F-I) performed on tissue from sqh^{AX3}, sqh::GFP flies.

Fig 4: Follicle cell divisions are biased towards tissue expansion but not interphase cell shape.

A) Cartoon demonstrating how the tissue expansion angle is determined.

B) i) Planar division orientation is initially random in the follicular epithelium, with a significant bias towards the egg chamber elongation axis evident at stage 6 (asterisk, p = 0.0031, Wilcoxon Signed Rank Test, Theoretical Mean of 45; p = 0.0218 when comparison to a randomly generated list of the same size). Number of cells analyzed: stage 2/3 n=16, stage 4 n=27 stage 5 n=30, stage 6 n=40. **ii)** Quantification of the angle of tissue expansion as calculated by vector addition of the minor and major axis of egg chambers. Number of egg chambers analyzed: stage 2/3 n=10, stage 4 n=15, stage 5 n=15, stage 6 n=10. **iii)** Quantification of cell elongation angles (as shown in E) with respect to the chamber elongation axis by stage from live egg chambers.

Number of cells analyzed: stage 2/3 n=18, stage 4 n=49 stage 5 n=64, stage 6 n=97. Bars represent mean and standard deviation.

C) Planar division orientation at Stage 6 correlates with tissue expansion in Fat2-shRNA and Pak-shRNA egg chambers. Mann Whitney test w^{1118} versus Pak shRNA p = 0.0094. Neither the Fat2-shRNA nor Pak-shRNA distributions are stastically different from random (Wilcoxon Signed Rank Test, Theoretical Mean of 45). Number of cells analyzed: w^{1118} n =97, Fat2-shRNA n=44, Pak-shRNA n=39. Egg chambers analyzed: w^{1118} n=40, Fat2-shRNA n=21, Pak-shRNA n=21.

D) Neighboring cells can form new attachments underneath (basal to) a mitotic cell that has moved apically. Scale bars = 5 μm. Thin yellow lines in the XZ reconstructions indicate the z-position of the two XY focal planes.

E) Workflow for determining follicle shape shapes. Segmentation of an egg chamber with an aspect ratio of 1.5 reveals that follicle cell elongation is usually perpendicular to the elongation axis of the egg chamber. Cell outlines were marked with Basigin::YFP. Scale bars = 5 μm.

F) Live confocal imaging shows that the long axis of a follicle cell at interphase does not predict the orientation of division. Long axis orientations at the timepoints shown were determined as in (E). Scale bars = 5 μm.

G) The interphase long axis does not correlate with the division angle in both the follicular epithelium (FE) and embyronic neuroectoderm (ENE). n=10 cells (FE), 18 cells (ENE).

Fig 5: Mud does not determine planar spindle orientation in the FE.

A) The vertex long axis of cells does not correlate with the division angle in both the FE or ENE. The cell vertex distribution at interphase using both the vertex bipolarity and a modified method that takes into account the distance that vertices lie from cell barycentres (modified vertex bipolarity) does not predict the division angle. n=10 cells (FE), n=18 cells (ENE). Bars represent mean and standard deviation.

B, C) Pins and Mud are symmetric around the entire cell cortex in (B) mitotic follicle cells and (C) mitotic cells in the ENE. (B' and C') Confocal imaging of immunostained fixed tissue. Scale bars = 5 μm.

D) Planar division orientation in the follicular epithelium is independent of Mud. Division angles were calculated relative to the elongating axis of the egg chamber using an unbiased analysis tool. Number of cells analyzed: w^{1118} n=52; mud^3/mud^4 n=43; Random number generator n=50; Mean division angle w^{1118}= 31.6°, mud^3/mud^4= 30.9°, Random number generator = 46°; Wilcoxon Signed Rank Test, Theoretical Mean of 45, w^{1118} $p < 0.0001$, mud^3/mud^4 $p = 0.0003$, Random number generator $p = 0.7779$. Spindle angles in mud^3/mud^4 egg chambers are not significantly different from w^{1118} ($p = 0.7859$, Mann Whitney test). Spindle angles in w^{1118} and mud^3/mud^4 egg chambers are statistically different from the randomly generated list ($p = 0.006$ and $p = 0.0044$, Mann Whitney test).

E) Live imaging reveals a mitotic spindle rotating in the plane of the FE until anaphase at timepoint 0. Timepoints shown in minutes relative anaphase. Scale bars = 5 μm.

F) The variance in mitotic spindle angle in the ENE reduces as cells approach metaphase. Graph shows root mean square of spindle angles approaching metaphase (defined at t = 0 secs). Number of cells analyzed= 22.

Fig 6: Apical actomyosin shows a dynamic relocalization during early egg chamber development.

A, B) Live confocal imaging of Myosin-II shown by Zipper::YFP (A) and Spaghetti squash-mCherry (B) at the apical cortex of follicle cells during egg chamber elongation showing a transition from cell to tissue-level organization during stage 6. (B) The localization Sqh-mCherry is shown relative to adherens junction marked by Shg::GFP.

Fig 7: Canoe disruption disrupts spindle orientation, Myosin organization and tissue packing.

A) Apical Myo-II localization as marked by Sqh-GFP is disrupted in round (stage 2/3) and elongated (stage 6) egg chambers. Red arrows point to the seperation of Myo-II at cell junctions,

indicating that actomyosin is no longer correctly linked to adherens junctions. Live confocal imaging. Scale bars = 5 μm.

B) Planar division orientation in the follicular epithelium is dependent on apical tension in a Canoe-dependent manner, with Canoe-shRNA treated egg chambers showing a randomization of division orientation. Division angles were calculated relative to the elongating axis of the egg chamber using an unbiased analysis tool. Number of cells analyzed: w^{1118} n=52; Canoe-shRNA n=58; Random Number Generator n = 50. Mean division angle w^{1118}= 31.6°, Canoe-shRNA= 43.3°, Random number generator = 46°; Mann Whitney test versus w^{1118}: Canoe-shRNA p = 0.0345 ; Wilcoxon Signed Rank Test, Theoretical Mean of 45, w^{1118} p < 0.0001, Canoe-shRNA p = 0.7411, Random number generator p = 0.7779. Bars represent mean and standard deviation.

C) Sidedness is affected by planar division orientation in an in silico simulated epithelium. One round of doubling extending over a six-hour period was simulated in a stretched tissue under different conditions for division orientation. The three time points shown reflect cell geometry in the first two hours (early), second two hours (mid), and last two hours (late).

D, E) Tissue topology is affected by disruption of Canoe, but not Mud. (D) Statistical significance for cell side distributions was calculated using a chi-squared test. Number of cells analyzed: w^{1118} 1.4-1.6 n=284; Canoe-shRNA 1.4-1.6 n=310; mud^3/mud^4 1.4-1.6 n=251. (E) Representative image of a Canoe-shRNA follicle epithelium. Cell outlines are marked with Basigin::YFP. This egg chamber has no mitotic cells and AR of 1.58. Scale bars = 5 μm.

Fig 8: A model for division orientation in the follicular epithelium.

Orientation is achieved separately in the apical basal and planar axes. Pins/Mud in green, Apical actomyosin in red, microtubules in blue.

Expanded View Figure Legends

Expanded View Fig 1: Inhibition of cell division reduces cell number without affecting egg chamber morphogenesis.

A) Visual workflow of image analysis for cell geometry calculations.

B) Irregular cell height in a stage 2 wildtype egg chamber. Confocal imaging of fixed tissue. Scale bar = 5 μm.

C) The number of cells around the circumference in egg chambers of increasing aspect ratio is altered by disruption of String. Bars represent mean and standard deviation. Egg chambers analyzed: w1118 1.0-1.2 n=13, 1.2-1.4 n=10, 1.4-1.6 n=11; String shRNA 1.0-1.2 n=8, 1.2-1.4 n=7, 1.4-1.6 n=6.

D) Egg chamber elongation over developmental time is unchanged by String depletion. Number of egg chambers analyzed: w^{1118}: stage 2/3 n=10 stage 4 n=15, stage 5 n=15, stage 6 n=10. String-shRNA stage 2/3 n=3, stage 4 n=13, stage 5 n=17, stage 6 n=10.

E,F) Tissue defects, including (C) gaps and (D) cells of irregular height are observed in later stage egg chambers after String depletion. The start of the gap in (C) is indicated with an arrowhead. Scale bars = 5 μm.

Expanded View Fig 2: Quantification of the biophysical and geometrical properties of egg chambers.

A) Follicle cell heights in w^{1118} and String-shRNA egg chambers at different aspect ratios. Number of cells analyzed: w^{1118} 1.0-1.2 n=17, 1.2-1.4 n=11, 1.4-1.6 n=10; String shRNA 1.0-1.2 n=9, 1.2-1.4 n=11, 1.4-1.6 n=10. Error bars represent standard deviation.

B) Cartoon demonstrating the location of laser cuts performed in sagittal view. Pole cuts were not performed over pole cells, as these cells exhibit enrichment of actomyosin at their cortex.

C) Kymographs for representiative apical cut experiment shown in Fig 3 H and I. Yellow lines indicate size of cut site at the first timepoint post-ablation as a guide to show recoil of the cut edge.

D) Paired datapoints from the experiment in Fig 3I showing recoil speeds in AP versus UD.

E) Recoil is not higher towards either axis on average in stage 4 and 5 egg chambers with aspect ratios of less than 1.3. Graph shows the ratio of recoil speed plotted on a $\log_2$ scale in the AP

versus the UD axis. Red line at x=1 indicates equal recoil in both axes. Values above 1 indicate higher recoil speeds in the AP axis lower than 1 indicate higher recoil in the UD axis. AP/UD Ratio Median = 0.9884 ; Mean = 0.9871. Wilcoxon Signed Rank Test to test for significance of the recoil ratio AP/UD shows that the median is significantly different from 1 to p = 0.8438. Number of cuts = 8. Bar represents median.

F) Cell divisions occur at all positions in the egg chamber. Top - a model egg chamber is split into quartiles, with both the relative surface area at each quartile and the number of divisions (n = 165) observed in that quartile. Bottom - positions were determined relative to the anterior pole, on a normalized scale of 0 (anterior) to 100 (posterior). The mean average position is 57^{o}, consistent with the observation that egg chambers are slightly larger (have more total cells) at the posterior.

G) i) Planar division orientation bias is reduced in Fat2 egg chambers at stage 6. (stage 2/3 n=16, stage 4 n=29, stage 5 n=42, stage 6 n=44.) **ii)** Quantification of the angle of tissue expansion as calculated by vector addition of the minor and major axis of egg chambers. (stage 2/3 n=7, stage 4 n=17, stage 5 n=29, stage 6 n=21.) **iii)** Quantification of cell elongation angles with respect to the chamber elongation axis by stage from live egg chambers. (stage 2/3 n=18, stage 4 n=50 stage 5 n=89, stage 6 n=100.)

H) Fat2-shRNA and Pak-shRNA egg chambers exhibit a defect in elongation at stage 6. (Unpaired t-test with Welch's correction). Number of egg chambers analyzed: w^{1118} n= 10, Fat2-shRNA n=23, Pak-shRNA n=21.

I) The orientation of follicle cell long axes correlates with the extent of follicle cell elongation (cell aspect ratio). Put another way, the longer the cell, the more likely it is to be oriented perpendicular to the elongating axis of the egg chamber. Spearman rank correlation test elongation p = 0.0003. In this graph, cells quantified in (C) were binned into elongation groups to facilitate comparison. Average angles in the three longest groups differ from random (Wilcoxon Signed Rank Test). Correlation between long axis and spindle angle is also observed, as described in the text. Number of egg chambers analyzed: w^{1118} n= 10.

J) Interphase cell elongation is biased away from the elongating axis of the egg chamber. Number of cells: 1.0-1.2 n=23, 1.2-1.4 n=76, 1.4-1.6 n=114.

Data information: Bars represent mean and standard deviation.

Expanded View Fig 3: Planar cell division orientation in the follicular epithelium and embryonic neurectoderm are independent of cell shape cues and the canonical spindle orienting machinery.

A) The vertex long axis of cells does not correlate with the division angle in both the FE or ENE. The cell vertex distribution at metaphase using both the vertex bipolarity and a modified method that takes into account the distance that vertices lie from cell barycentres (modified vertex bipolarity) does not predict the division angle. n=10 cells (FE), n=18 cells (ENE). Bars represent mean and standard deviation.

B) Gliotactin immunoreactivity is not observed in the FE.

C) The imaginal wing disc, in which Gliotactin localizes to cell vertices, is used as a control.

D) Fixed images show that Pins and Mud-GFP colocalize around the cell cortex in mitotic follicle cells. These results confirm the live imaging shown in Fig 4A. (D') A fixed image of Pins-YFP alone. Scale bar = 5 μm.

E) Planar division orientation in the follicular epithelium is independent of Mud using a second method of knock-down. Division angles were calculated relative to the elongating axis of the egg chamber using an unbiased analysis tool. Number of cells analyzed: w^{1118} n=52; Mud-shRNA n=58, Random number generator n=50; Mean division angle w^{1118}= 31.6º, Mud-shRNA= 33.7º, Random number generator = 46º; Mann Whitney test versus w^{1118}: Mud-shRNA $p = 0.898$, Wilcoxon Signed Rank Test, Theoretical Mean of 45, w^{1118} $p < 0.0001$, Mud-shRNA $p < 0.0001$, Random number generator $p = 0.7779$. Bars represent mean and standard deviation.

F) Quantification of mitotic spindle angle in the ENE with respect to angle at metaphase. Quantifications from live confocal movies of embryos expressing Basigin-YFP, Tub-RFP, Cnn-RFP. Quantifications performed using 'Spindlometer' software. n=22.

G-I) Representative movies of mitotic spindle behavior from movies quantified in (F). Spindles exhibit both little/no rotation (G) and large rotations and rocking (H and I) in planar orientation. Individual spindle angle traces shown in (I). Scale bars = 5 μm.

Expanded View Fig 4: Characterization of apical junction protein localization in egg chambers.

A) Sqh-mCherry localizes to the apical cell cortex of the follicular epithelium, colocalizing with Shg::GFP. Live confocal tissue imaging.

B) Localization of Sqh-GFP at the apical and basal cortices of the follicular epithelium through development, showing that basal alignment of Myo-II fibers precedes the change in apical organization. Scale bars = 5 μm.

C) Apical Sqh-GFP localization in the embryonic epithelium in Stage 7 embryos exhibiting distinct medial and planar polarized junctional pools of Sqh shown as comparison to the localization pattern found in the follicular epithelium (B). Scale bar = 5 μm.

D) "Blobs" of Sqh::Cherry at the medial cell cortex usually colocalize with the ring canal marker Pavarotti-KLP::GFP.

E-H) Shotgun (E), Armadillo (F), Canoe (G), and Ajuba (H) are all found symmetrically localized at adherens junctions across apical cell junctions in the follicular epithelium at stage 6. Quantification of fluorescence intensity of all four fails to show any planar polarity in junctional localization. Ordinary one-way ANOVA to test for differences: Shg::GFP $p = 0.3695$, Cno-GFP $p = 0.1192$, Arm-GFP $p = 0.7282$, Jub::YFP $p = 0.8756$. Number of junctions used for analyisis Shg n=270, Cno n=173, Arm n=147, Jub n=236. Bars represent mean and standard deviation.

Data information: All images from confocal live imaging.

Expanded View Fig 5: Canoe does not regulate the position of the mitotic spindle in the epithelial apicobasal axis.

A) Planar division orientation in the follicular epithelium is unaffected by Shg shRNA. Division angles were calculated relative to the elongating axis of the egg chamber using an unbiased analysis tool. Bars represent mean and standard deviation. Number of cells analyzed: w^{1118} n=52; Shg-shRNA n=44; Mean division angle w^{1118}= 31.6°, Shg-shRNA= 35.6°. Mann Whitney test versus w^{1118}: p = 0.3773, Wilcoxon signed rank test, theoretical mean of 45, w^{1118} p < 0.0001, Shg-shRNA p < 0.0117.

B) Apical-basal spindle orientation is not disrupted in mitotic clones mutant for the null allele cno^{R2}. mud^3/mud^4 egg chambers are used as a positive control. Bars represent mean and standard deviation. Number of cells analyzed w^{1118} n=19, $cno^{R2}/+$ n=17, cno^{R2}/cno^{R2} n=14, mud^3/mud^4 n=13. Panels (B' and B'') show representative spindles in cno^{R2} and mud^3/mud^4 mutant cells. The mutant clone is marked by the absence of nls-RFP. Scale bars = 5 μm.

C) Canoe is not proximal to the spindle in mitotic follicle cells. The mitotic cell is outlined in the white box. Scale bar = 5 μm.

D) Canoe-shRNA depletes Canoe expression in the FE. Canoe-shRNA was driven in a mitotic clone, which is marked by GFP. Canoe immunoreactivity is not observed in the clone.

E) Egg chamber elongation is not affected by disruption of Canoe or Mud. Bars represent mean and standard deviation. Number of egg chambers analyzed w^{1118} 1.0-1.2 n=24, 1.2-1.4 n=14, 1.4-1.6 n=18; Canoe shRNA 1.0-1.2 n=20 1.2-1.4 n=15 1.4-1.6 n=24; mud^3/mud^4 1.0-1.2 n=24 1.2-1.4 n=14; 1.4-1.6 n=15.

F) Average cell size decreases by half after one round of doubling over six hours in a simulated in silico epithelial tissue undergoing stretch. Cell size in this simulation is not affected by the planar orientation of division. The three time points shown reflect sizes in the first two hours (early), second two hours (mid), and last two hours (late). The model was run post-hoc and not in an attempt to systematically fit model parameters to the data, or base our argument on a direct quantitative comparison to the data and hence the model was run n=1. Bars represent mean and standard deviation.

G) Follicle cell size measurements in control, Canoe-shRNA, and mud^3/mud^4 egg chambers of different aspect ratios. These measurements were derived from at least three egg chambers from at least three flies per AR range. Bars represent mean and standard deviation. w^{1118} 1.0-1.2 n=24, 1.2-1.4 n=14, 1.4-1.6 n=18; Canoe shRNA 1.0-1.2 n=20, 1.2-1.4 n=15, 1.4-1.6 n=24; mud^3/mud^4 1.0-1.2 n=21, 1.2-1.4 n=14, 1.2-1.4 n=15.

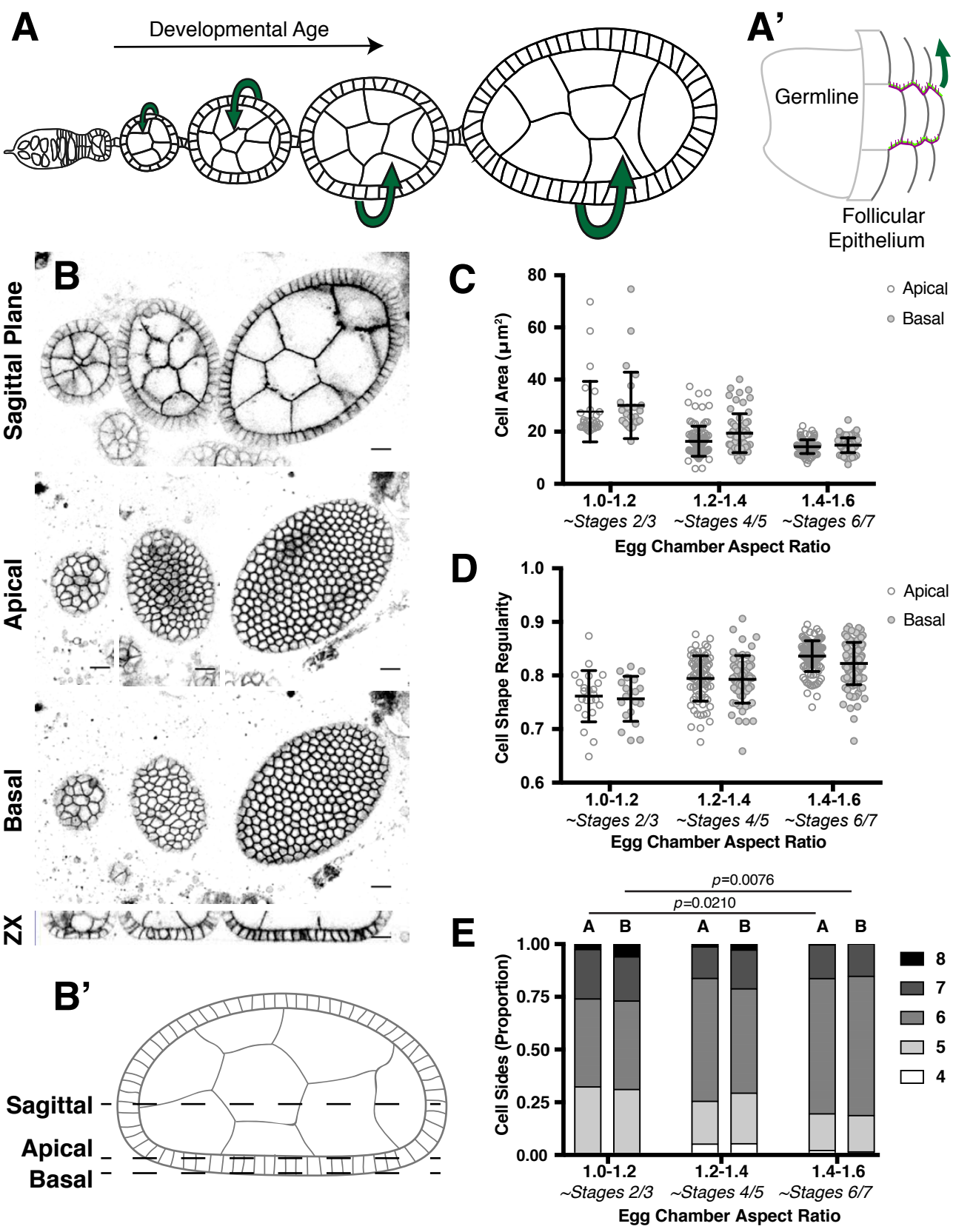

Figure 1 - Finegan *et al*

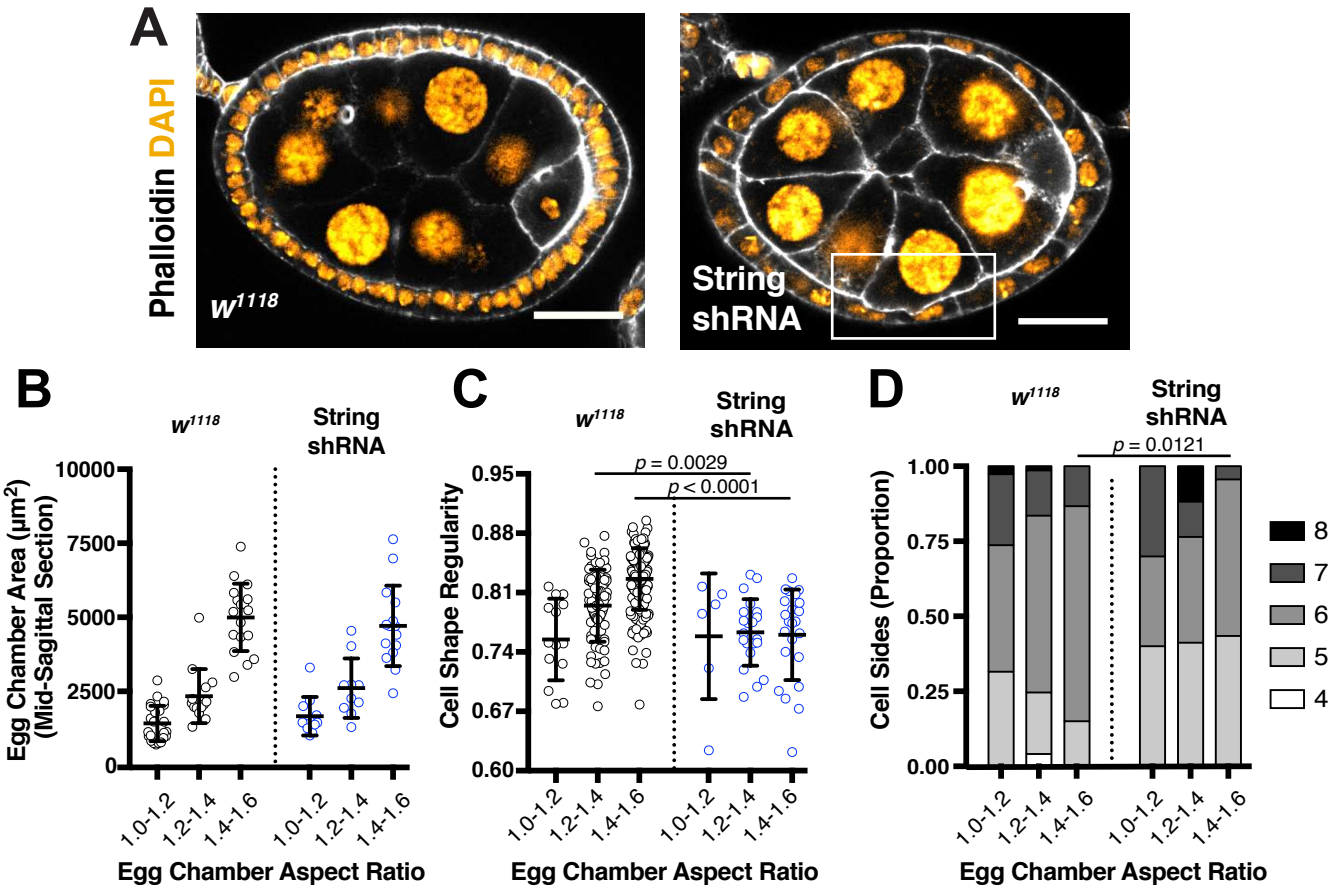

Figure 2 - Finegan *et al*

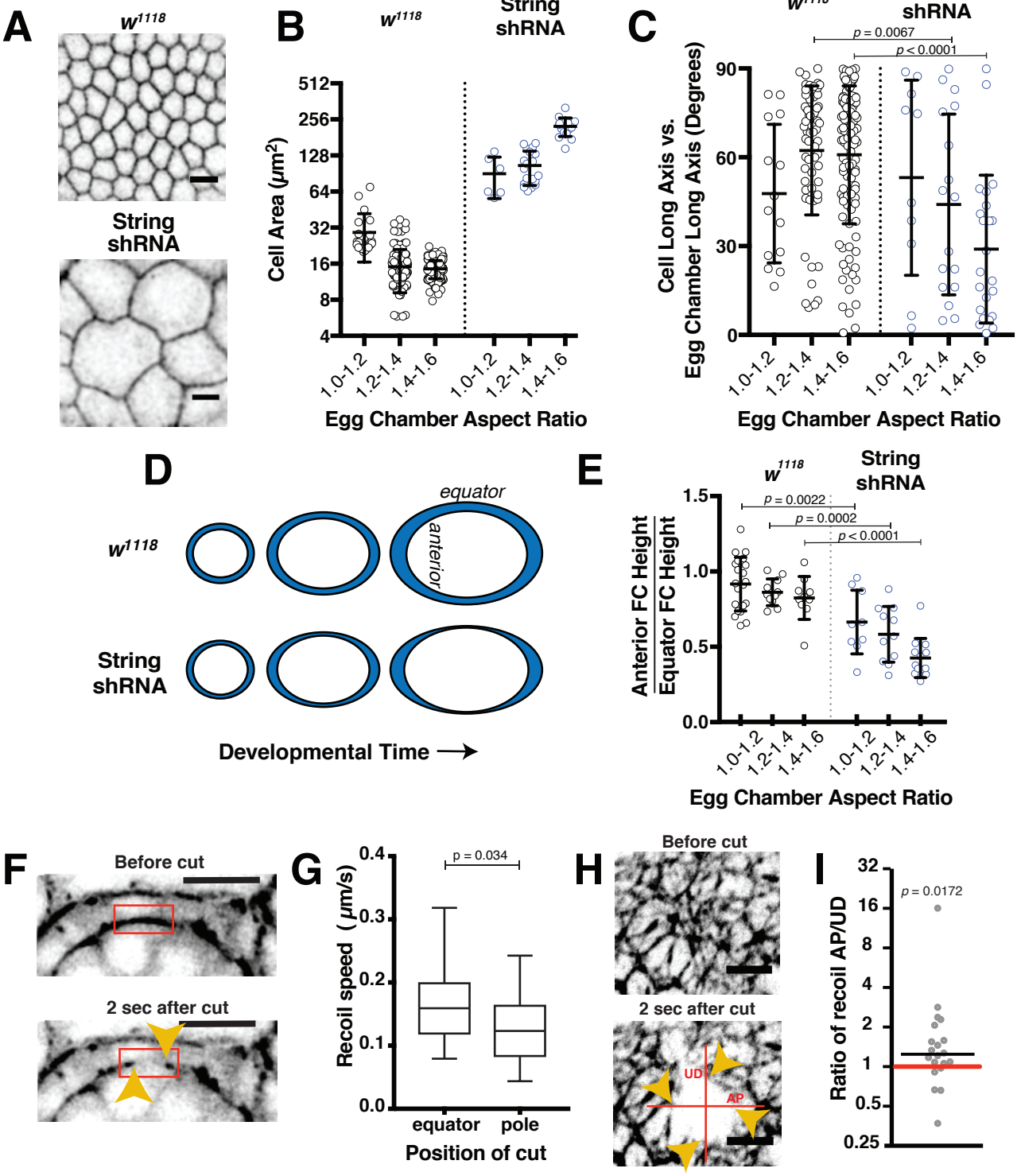

Figure 3 - Finegan *et al*

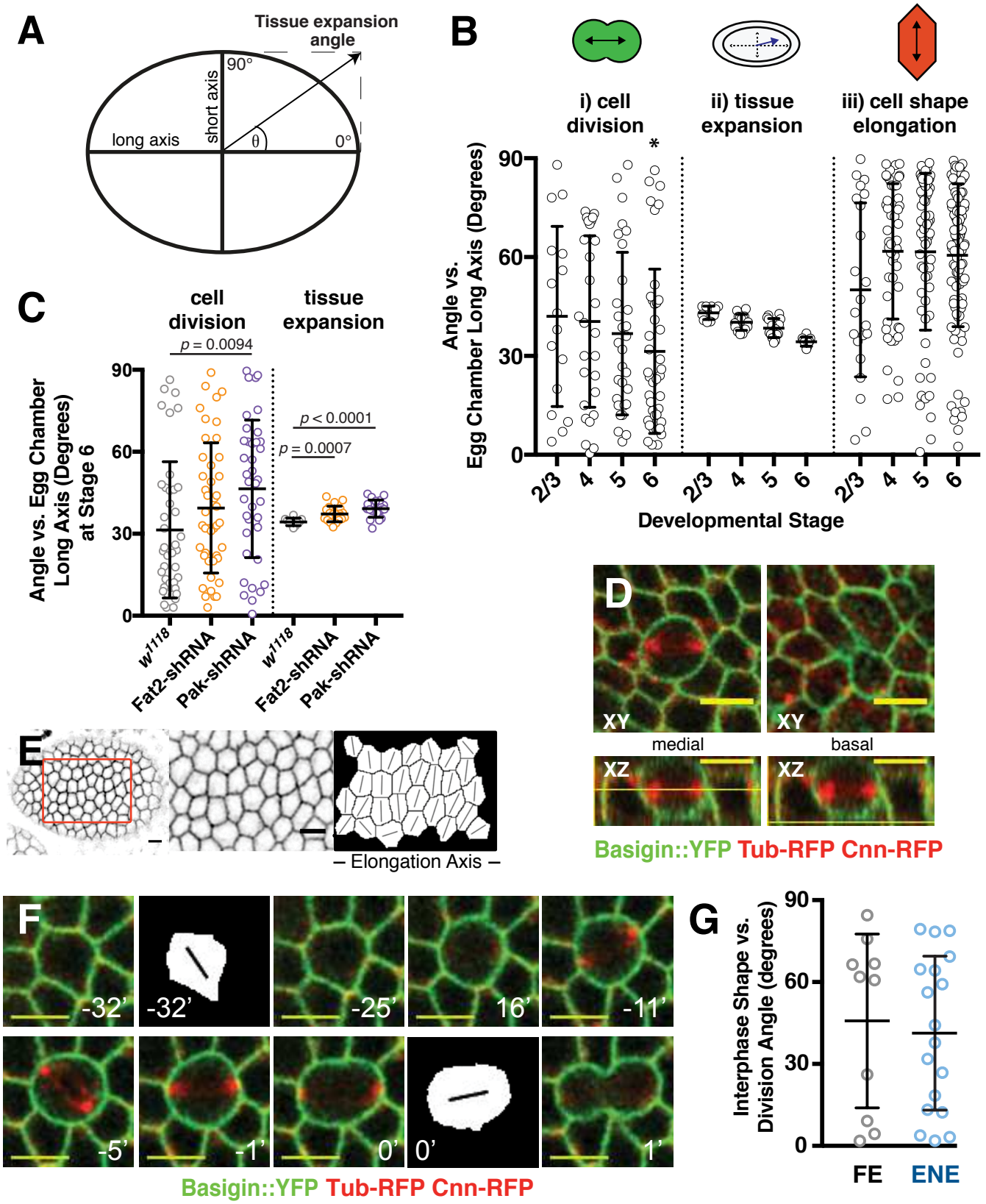

Figure 4 - Finegan *et al*

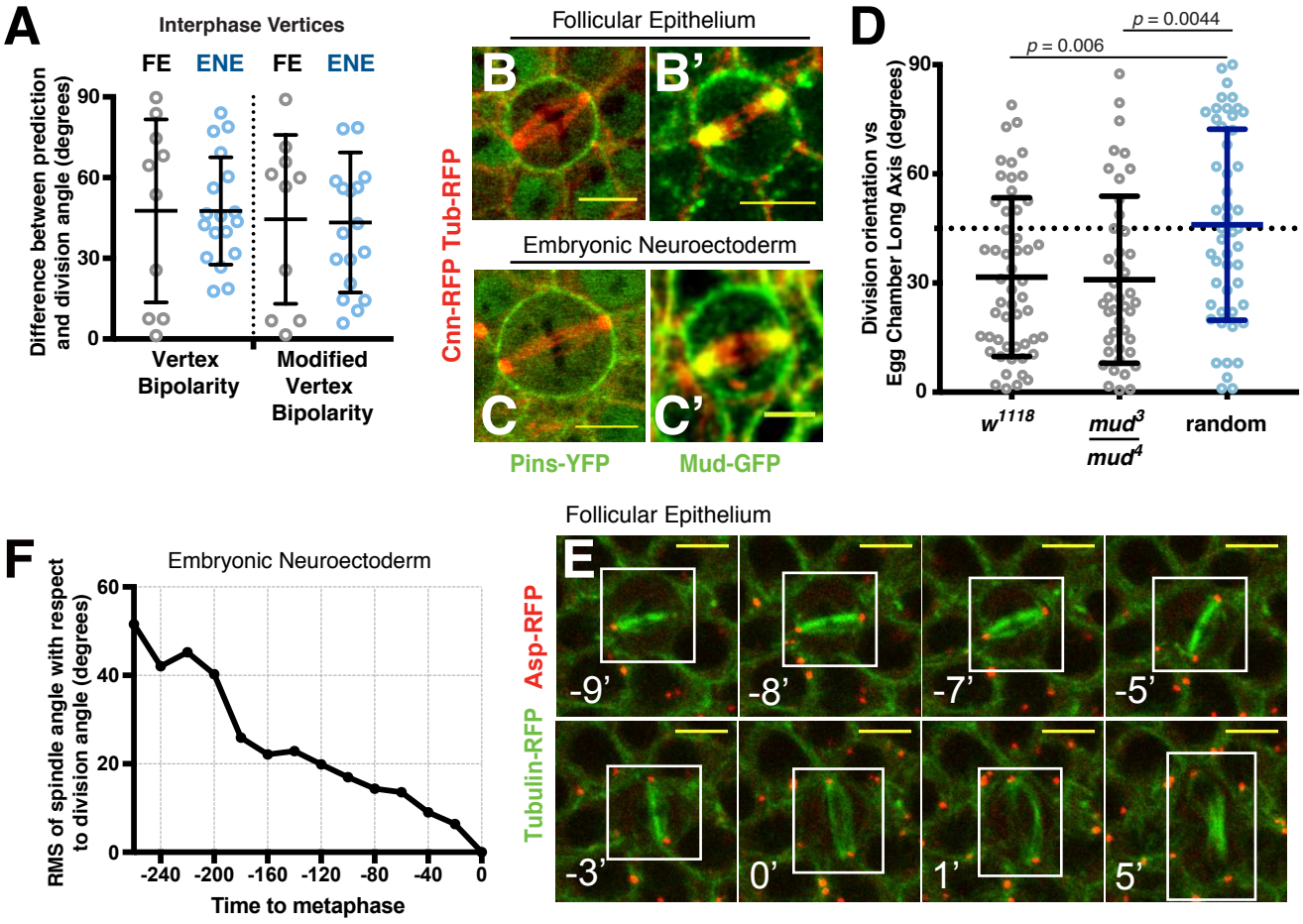

Figure 5 - Finegan *et al*

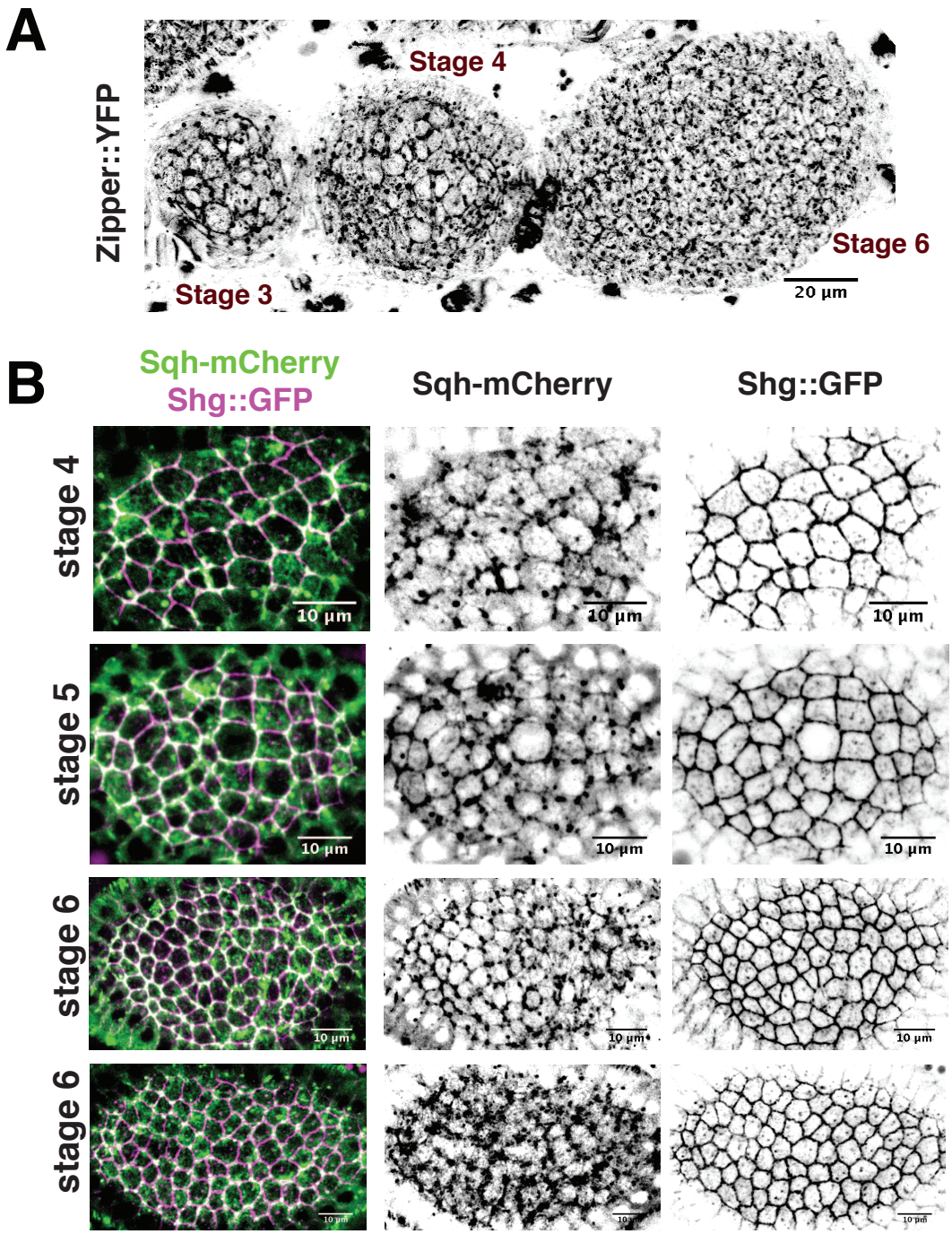

Figure 6 - Finegan *et al*

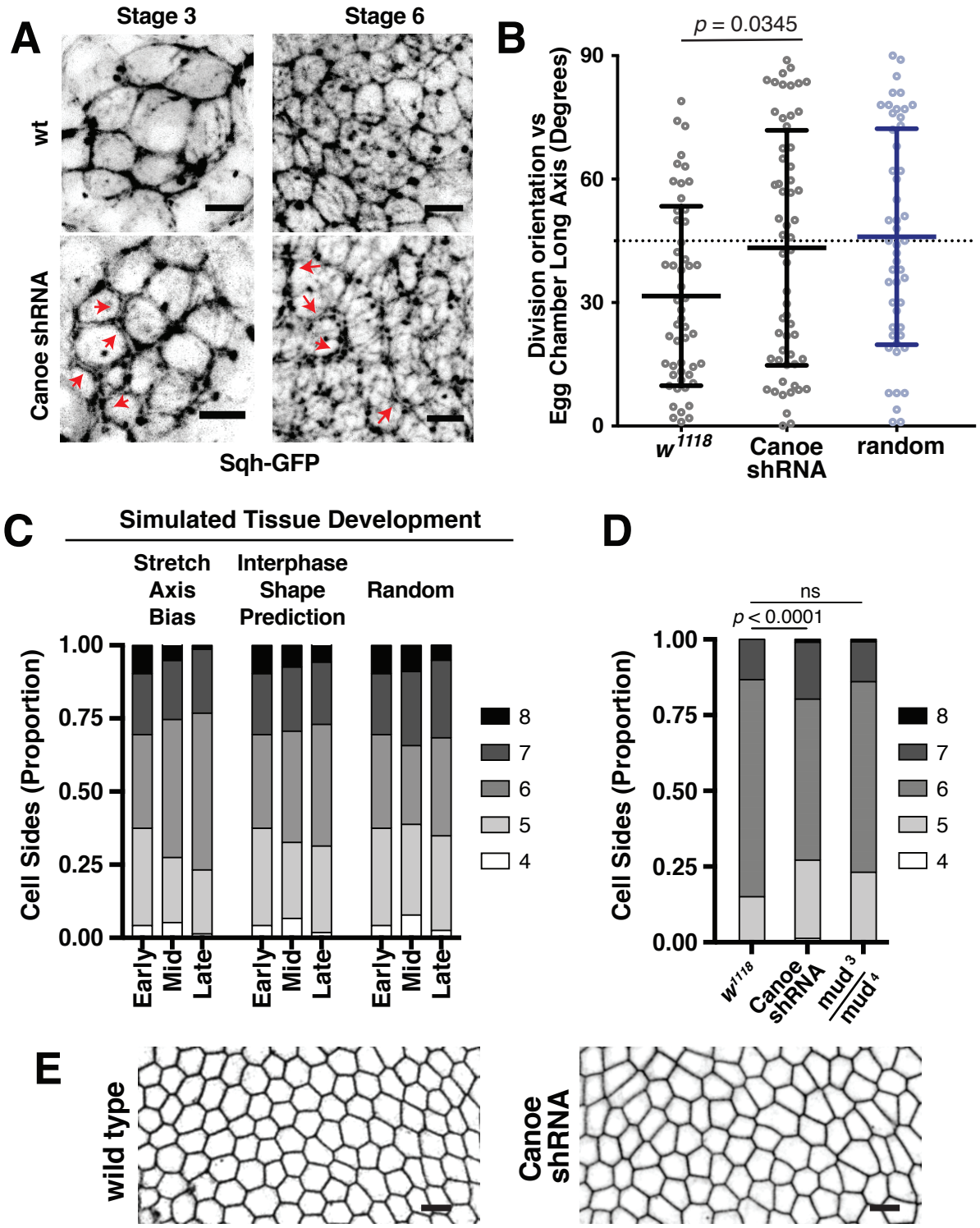

Figure 7 - Finegan *et al*

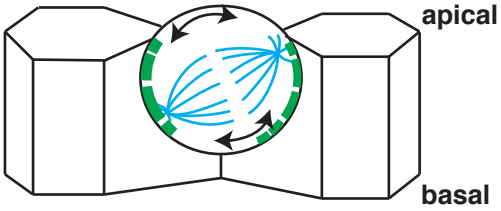

Apicobasal positioning
relies on Pins/Mud to
exert a cortical pulling force
on astral microtubules

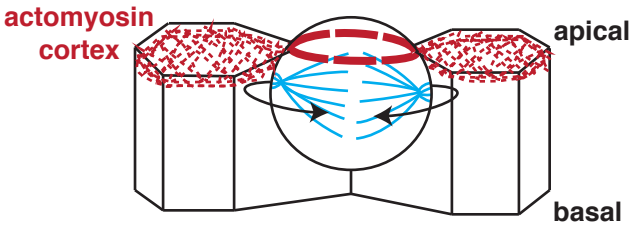

Planar positioning
relies on
apical cortical tension but is
Pins/Mud independent

Figure 8 - Finegan *et al*

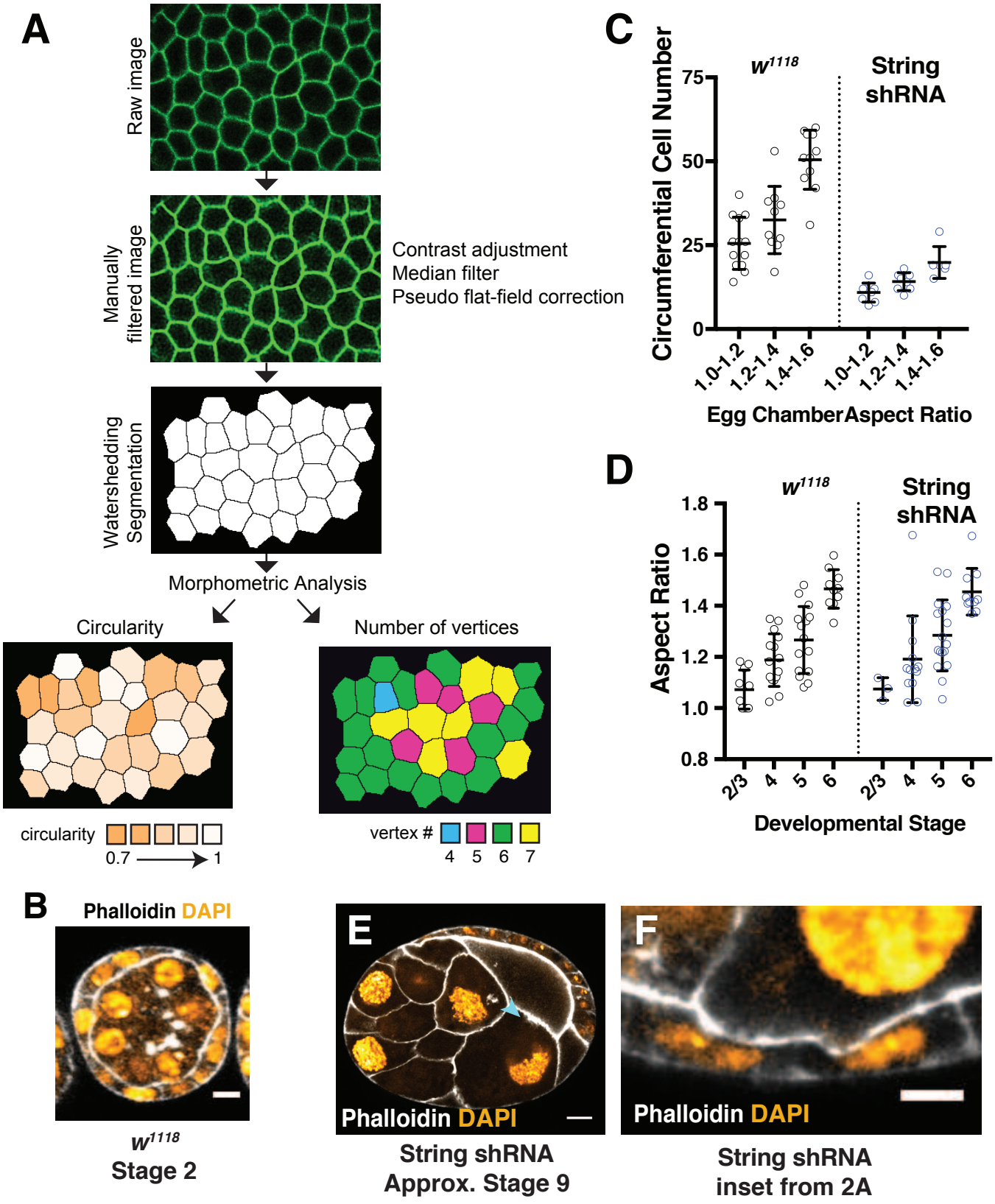

Figure EV1 - Finegan *et al*

Figure EV2 - Finegan *et al*

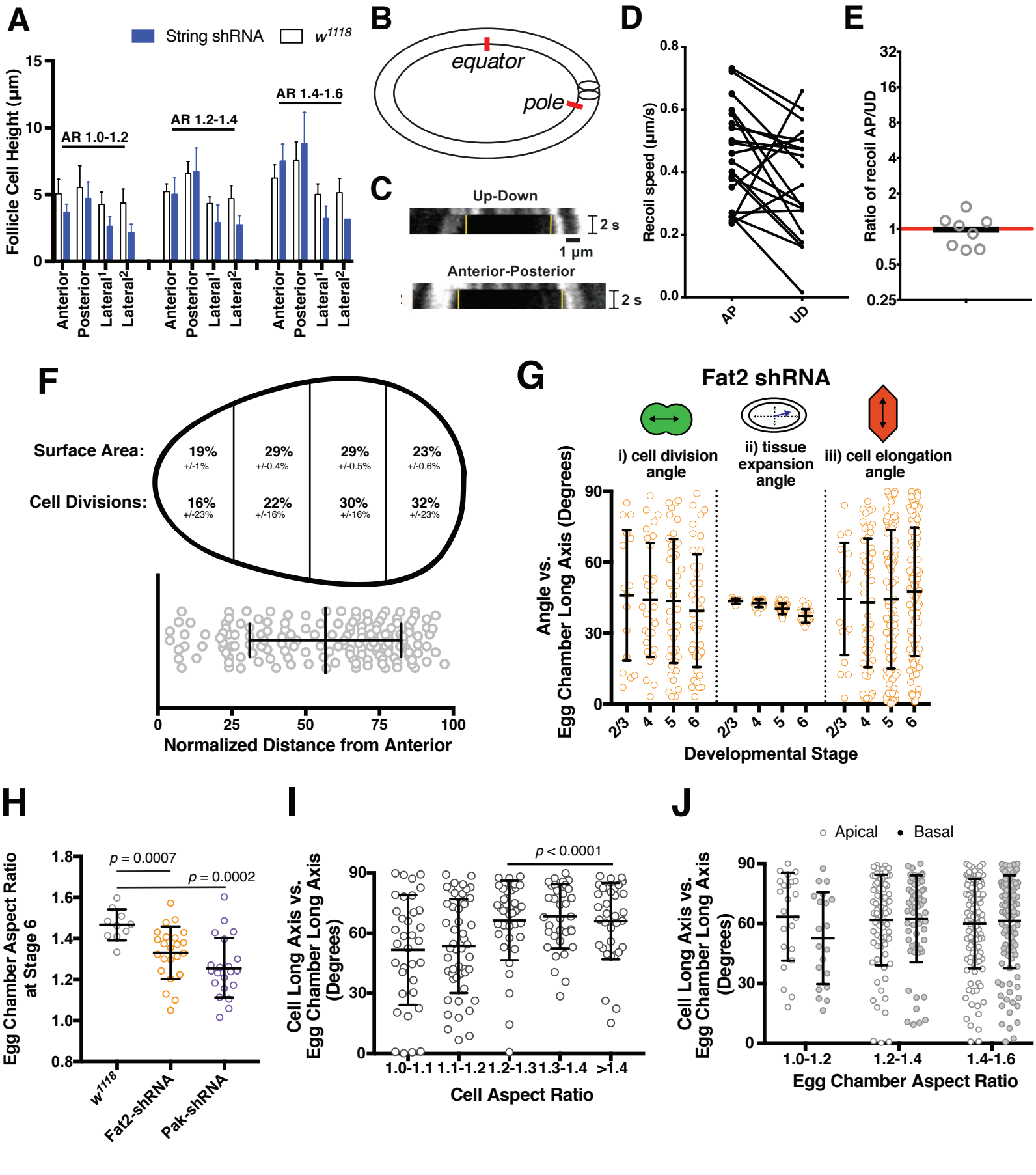

Figure EV3 - Finegan *et al*

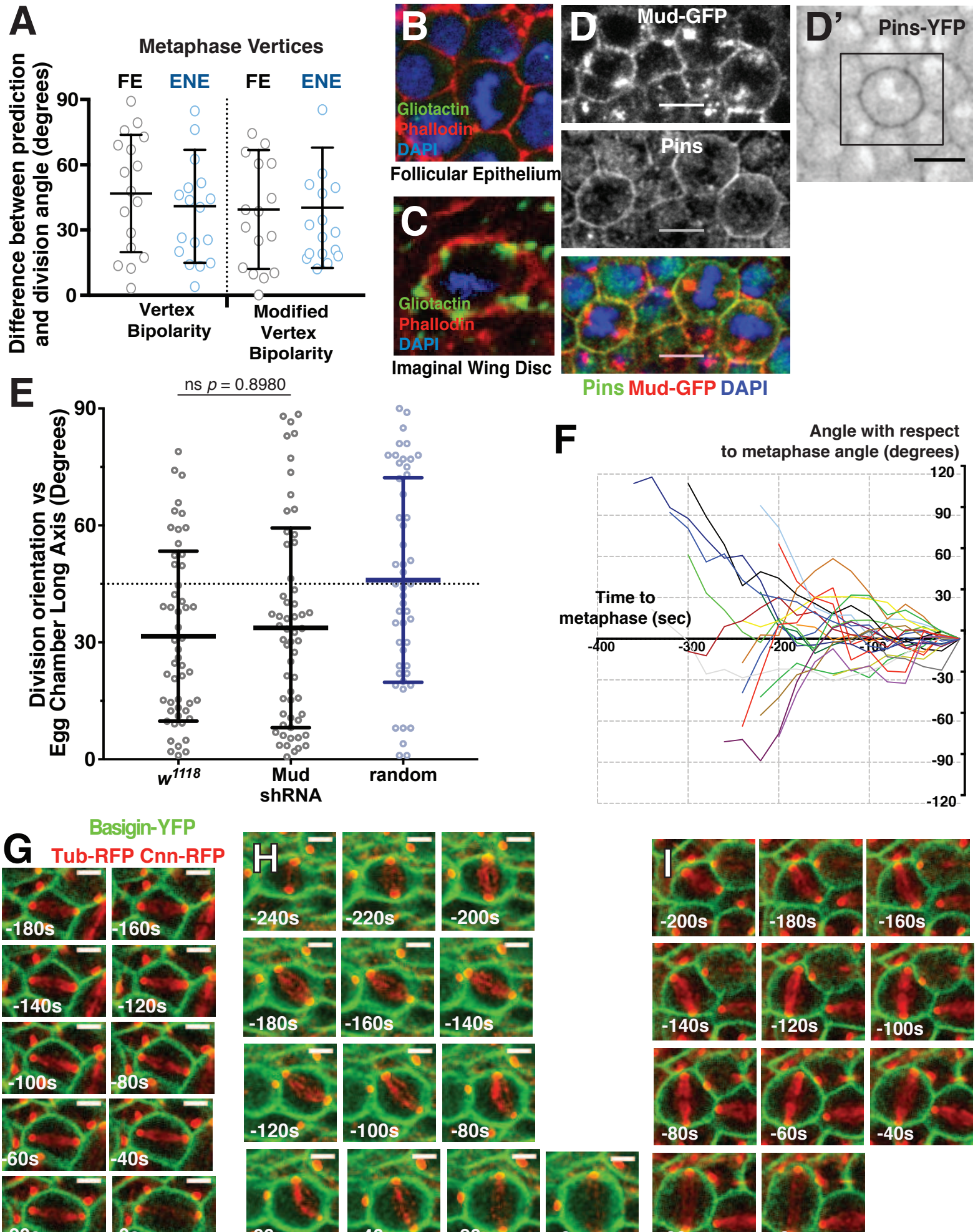

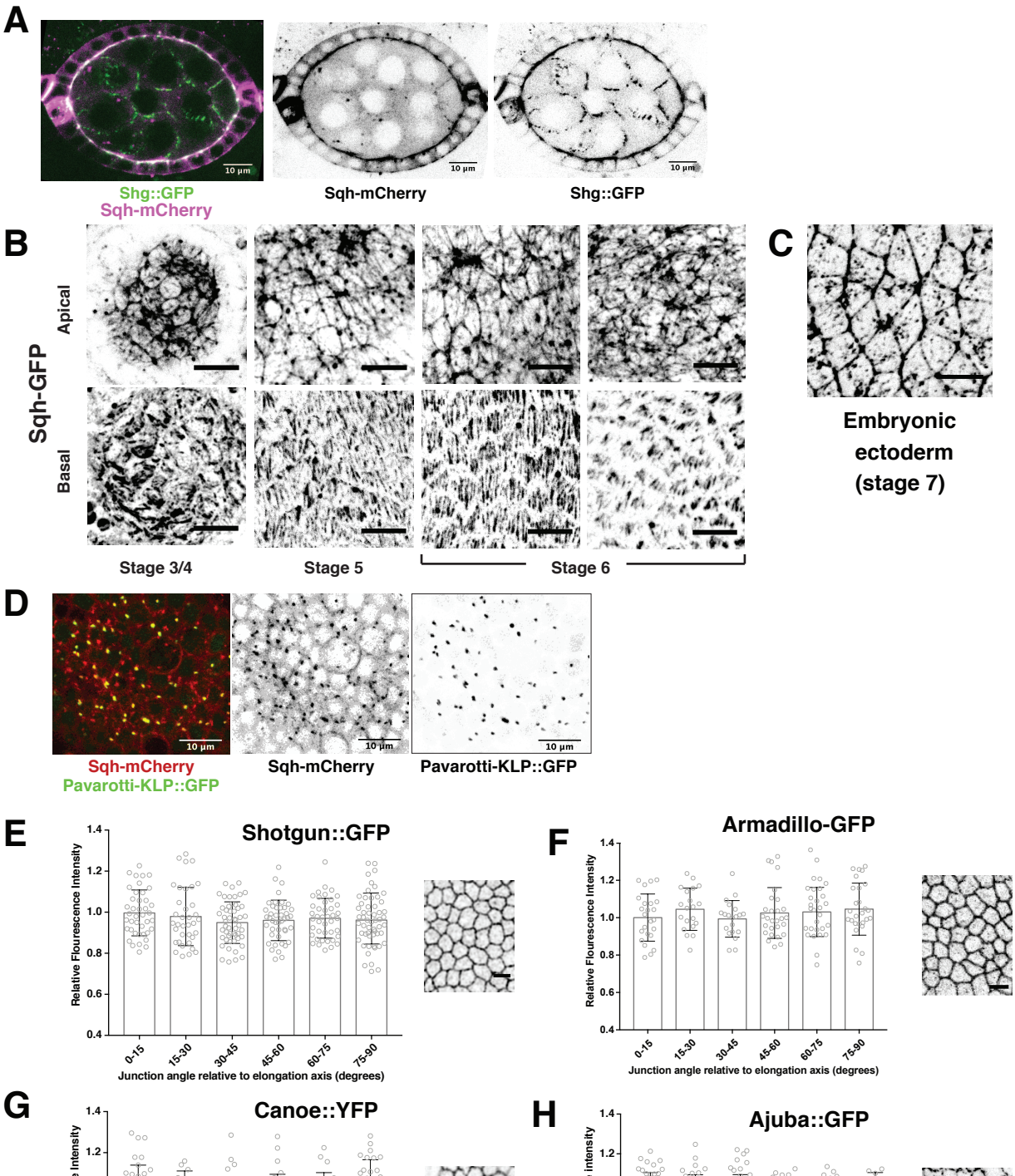

Figure EV4 - Finegan *et al*

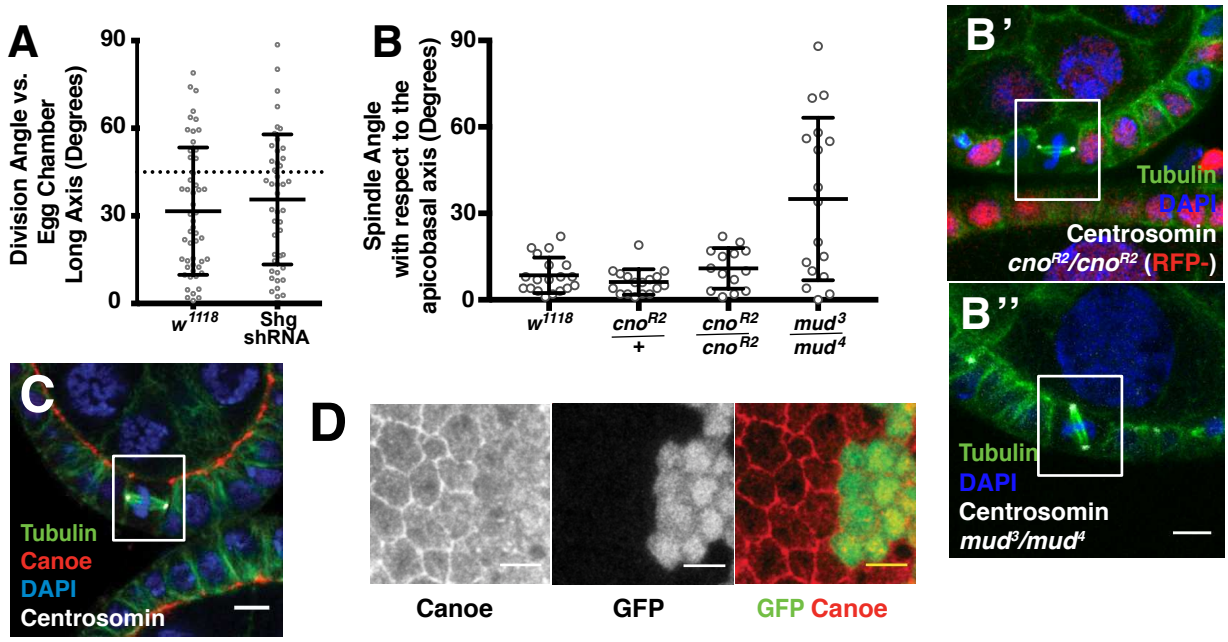

Figure EV5 - Finegan *et al*